RSC Chemical Biology

ROYAL SOCIETY OF CHEMISTRY

REVIEW

View Article Online
View Journal | View Issue

Open Access Article. Published on 24 kovo 2021. Downloaded on 2026-01-19 22:31:07.
This article is licensed under a Creative Commons Attribution-NonCommercial 3.0 Unported Licence.

Check for updates

Cite this: *RSC Chem. Biol.*, 2021, **2**, 743

Recent development of near-infrared photoacoustic probes based on small-molecule organic dye

Chonglu Li,†[ab] Chang Liu,†[bc] Yifan Fan,†[c] Xin Ma,[d] Yibei Zhan,*[a] Xiaoju Lu*[a] and Yao Sun*[c]

Received 5th December 2020,
Accepted 7th March 2021

DOI: 10.1039/d0cb00225a

rsc.li/rsc-chembio

Photoacoustic imaging (PAI), which integrates the higher spatial resolution of optical imaging and the deeper penetration depth of ultrasound imaging, has attracted great attention. Various photoacoustic probes including inorganic and organic agents have been well fabricated in last decades. Among them, small-molecule based agents are most promising candidates for preclinical/clinical applications due to their favorite *in vivo* features and facile functionalization. In recent years, PAI, in the near-infrared region (NIR, 700–1700 nm) has developed rapidly and has made remarkable achievements in the biomedical field. Compared with the visible light region (400–700 nm), it can significantly reduce light scattering and meanwhile provide deeper tissue penetration. In this review, we discuss the recent developments of near-infrared photoacoustic probes based on small molecule dyes, which focus on their "always on" and "activatable" form in biomedicine. Further, we also suggest current challenges and perspectives.

1. Introduction

Biomedical imaging techniques, due to the non-invasive visualization and quantification biological processes in intact living biology, have received tremendous attention in preclinical and clinical investigations.[1–4] Over the years, various imaging modalities such as magnetic resonance imaging (MRI), positron emission tomography (PET), ultrasound (US) imaging, and optical imaging have been well demonstrated in the biomedical field.[5–11] Among them, optical imaging provides real-time anatomical and information at high spatiotemporal resolution and high sensitivity with invasiveness, yet its penetrating depth is down to ~0.1 mm.[12–14] Therefore, it is still a troublesome task to use pure optical imaging for achieving high spatial resolution at centimeter depths before the advent of photoacoustic imaging (PAI).[15]

PAI is an emerging and non-invasive hybrid imaging modality that combines the advantages of traditional optical imaging and US imaging, realizing high-resolution imaging with centimeter-level depth.[16–19] According to the photoacoustic effect theory first proposed by Alexander Graham Bell in 1881, biological tissues, endogenous chromophores, or exogenous contrast agents irradiated by a nanosecond-pulsed laser absorb light energy to produce a thermally induced pressure jump that emits broadband acoustic waves (Fig. 1a). Ultrasound transducers transmit the collected photoacoustic signals to a computer, thus reconstructing the light energy distribution map inside the tissue.[20–22] Owing to the scattering of ultrasound waves in the tissue, which is only 1/1000 that of light waves, the tissue penetration depth of PAI can achieve centimeter-level compared with traditional optical imaging.[23] Besides, PAI also provides non-invasive, speckle-free, and label-free imaging.[15,24] Due to these unique advantages, PAI has become the most promising biomedical imaging modality.[25–30]

Many endogenous chromophores in biological tissues can be used as contrast agents for photoacoustic imaging such as water, lipids, oxy/deoxyhemoglobin (HbO_2/Hb), and melanin (Fig. 1b).[31] The strongly absorbing hemoglobin in the visible region (400–650 nm) was used for vascular PAI. Due to biological tissues having a strong scattering and absorption of light emitted by a nanosecond pulsed laser, it is difficult for

[a] School of Chemistry and Chemical Engineering, Hubei Polytechnic University, Huangshi, 435003, China. E-mail: zhanyibei@163.com, xiaoju_lu@163.com
[b] Collaborative Innovation Center of Atmospheric Environment and Equipment Technology, Jiangsu Key Laboratory of Atmospheric Environment Monitoring and Pollution Control (AEMPC), Nanjing University of Information Science & Technology, Nanjing 210044, China
[c] Key Laboratory of Pesticides and Chemical Biology, Ministry of Education, International Joint Research Center for Intelligent Biosensor Technology and Health, Center of Chemical Biology, College of Chemistry, Central China Normal University, Wuhan 430079, China. E-mail: sunyaogbasp@mail.ccnu.edu.cn
[d] Guangdong Provincial Key Laboratory of Radioactive and Rare Resource Utilization, Shaoguan 512026, China
† These authors contributed equally to this work.

© 2021 The Author(s). Published by the Royal Society of Chemistry

Open Access Article. Published on 24 kovo 2021. Downloaded on 2026-01-19 22:31:07.
This article is licensed under a Creative Commons Attribution-NonCommercial 3.0 Unported Licence.

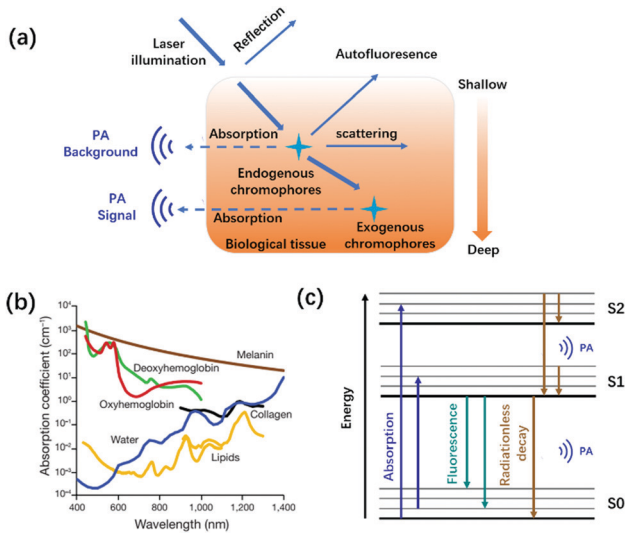

Fig. 1 (a) Schematic diagram of the interaction between light and tissue caused by the excitation light. (b) Absorption spectra of the main endogenous chromophores: oxyhemoglobin, red line; deoxyhemoglobin, green line; water, blue line; lipids, yellow lines; melanin, brown line; and collagen, black line. Adapted from ref. 22. Copyright© 2019 Springer Link. (c) Schematic diagram of photoacoustic signal generation.

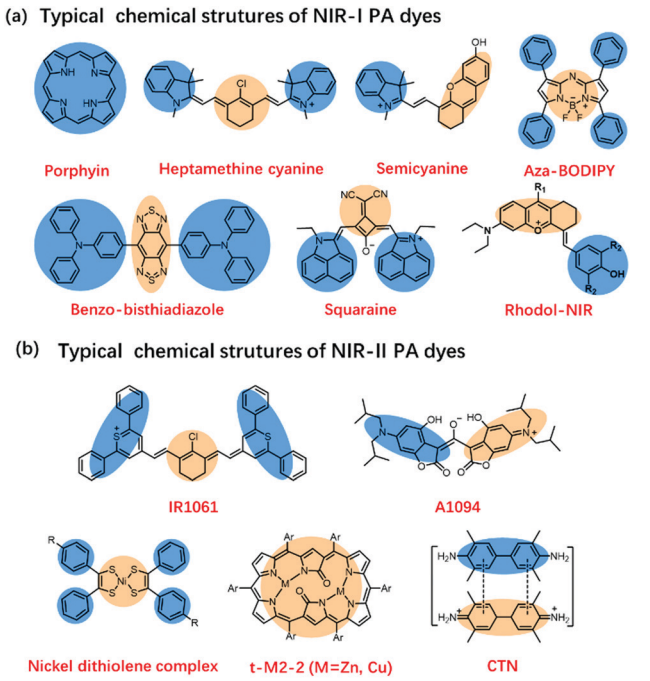

Fig. 2 (a) Typical chemical structures of NIR-I PA dyes. (b) Typical chemical structures of NIR-II PA dyes.

endogenous chromophores mainly located in the ultraviolet or visible region to perform the PAI of deep tissues.[32,33] To achieve a deeper penetration depth in biological tissues, exogenous contrast agents based on inorganic nanomaterial and organic molecules with absorption wavelengths in the near-infrared region (NIR, 700–1700 nm) have been developed for *in vivo* detection and imaging.[34–40] Compared with inorganic nanomaterials, small molecules provide a well-defined structure, rapid metabolism, low toxicity, and adjustable spectrum.[41–43] Besides, the PA signals of these small-organic molecules could be enhanced through structural modification.[44] Generally speaking, the design principles of PA dyes follows four points.[38,45] Firstly, after organic dyes were excited by a nanosecond-pulsed laser, it must pass through a fast non-radiative decay process (Fig. 1c). Secondly, organic dyes have more p-bonds or aromatic ring structures to achieve higher extinction coefficients. Thirdly, the introduction of molecular rotors in the organic dyes improves the PA signal by increasing the energy dissipation. Fourthly, organic dyes have a lower fluorescence quantum yield. Based on the above design principles, many small-molecule PA probes with excellent performance in NIR-I and NIR-II, such as porphyrin, cyanine, heptamethinecyanin, benzo bisthiadiazole, and nickel dithiolene complex have been reported in the last decade (Fig. 2).

Therefore, in this review, we summarized the recent development of near-infrared photoacoustic probes based on small-molecule organic dye. Firstly, we introduce the recent progress of "Always on" photoacoustic probes. Afterward, we highlight the recent advances in activatable photoacoustic probes for molecule detection and *in vivo* bioimaging. Finally, we elaborate on the challenges and perspectives of the near-infrared photoacoustic probes based on small-molecule organic dyes.

2. "Always on" photoacoustic probes

2.1 Single functional photoacoustic probes

Small-molecule dyes can not only can be applied for fluorescent imaging but also are very attractive candidates for PA imaging due to favorable circulation, excretion properties, and exhibiting feasible conjugation with targeting moieties. Some organic molecules such as heptamethine cyanine, BODIPY, squaraines, and benzo-bisthiadiazole dyes have been well explored for PAI.[46,47] In the decades of the rise in photoacoustic imaging, small-molecule probes were initially only used as a diagnostic reagent. For example, in 2008, Wang *et al.* firstly regarded Indocyanine green (ICG) as a PA contrast agent, applying it in the imaging of brain tumors in vivo.[47] They provided a new paradigm to high-resolution simultaneous molecular and functional imaging of intracranial brain tumors in small animal models.

To address the problem of small-molecule dyes with low solubility as well as a tendency to aggregate and photo-bleach, small-molecule dyes have always been modified with water-soluble polymer or encapsulated by amphipathic molecule such as DSPE-PEG, F-127. For example, in 2017, Saji *et al.* conjugated ICG with polysarcosine (PSar) and this approach not only addressed the problem of water-solubility but also forms nanoparticles to enhance the PA signal.[48] It demonstrated that this ICG-PSar nanosystem could achieve rapid tumor uptake, suggesting the active transport of PSar into the tumor tissues to further improve the targeting ability of the photoacoustic probes in tumors. In 2018, Poggi *et al.* reported ICG coupled to an integrin-binding vector PAI probe ICG-RGD. The *in vivo* PAI result indicated that target ligands such as

 © 2021 The Author(s). Published by the Royal Society of Chemistry

Open Access Article. Published on 24 kovo 2021. Downloaded on 2026-01-19 22:31:07.
This article is licensed under a Creative Commons Attribution-NonCommercial 3.0 Unported Licence.

RGD could both efficiently improve the water solubility and the retention time on the tumor region of ICG.[49]

To achieve a better signal-to-noise ratio (SNR) for *in vivo* imaging, the ratio PA probes have been developed. These probes can specifically detect the endogenous substance in the organism, thus also improving the SNR of photoacoustic imaging. It is worth mentioning that ratio probes possess the self-calibration system, thus cancelling out the interference from inside the organism. In 2018, Chen *et al.* designed Cu^{2+}-responsive NRh and non-responsive IR820, which formed NRh-IR-NMs *via* encapsulation with nanomichicelles (NMs) (Fig. 3a).[50] The part of NRh can realize Cu^{2+}-induced absorbance change, while the part of IR820 can act as the internal reference. They demonstrated that this ratio PA imaging probe has high selectivity and were a promising tool for Cu^{2+} detection (Fig. 3b). More recently, Fan *et al.* reported that a small-molecule probe (CyCl-1) can detect H_2S in the biomass (Fig. 3c).[51] They introduced active chlorine into the cyanine dyes, which can make it react with H_2S *via* nucleophilic reaction. It showed PA signals of 800 nm (attenuation) and 720 nm (enhancement) (Fig. 3d and e). With the increase in the HS^- concentration, the PA signal of the probe at 720 nm continued to increase, while the PA signal at 800 nm gradually decreased (Fig. 3f). Through the change in the ratio of the PA signal, the detection of H_2S at the physiological concentration level was successfully realized. Besides, the probe can be used to monitor the H_2S ratio PA in living mice, with high imaging fidelity and rapid clearance (Fig. 3g) to increase the penetration depth of photoacoustic imaging and reduce the interference of endogenous chromophores in biological tissues. In 2014, Zhang *et al.* chose squaraines as a contrast agent for PA imaging because they contain the character that has visible-light absorption in organic solvent and NIR-absorption after aggregation in water.[52] They show advanced red-shift effect and the albumin was added to squaraine dye as a protective carrier, successfully realizing squaraines for PA imaging in the NIR region. In 2020, Banala *et al.* found that 1H-pyrrole conjugation to BODIPY can induce red-shift and increase the signal of PAI.[53] They explained that the 1H-pyrrole is an electron-rich moiety, thus it can induce a red-shift in the absorption and fluorescence quenching *via* the photoinduced electron transfer (PET) process. Besides, metal–ligand coordination activity could also induce a significant red-shift in absorption than that of the free organic ligand due to the enhanced push–pull electron ability. In 2020,

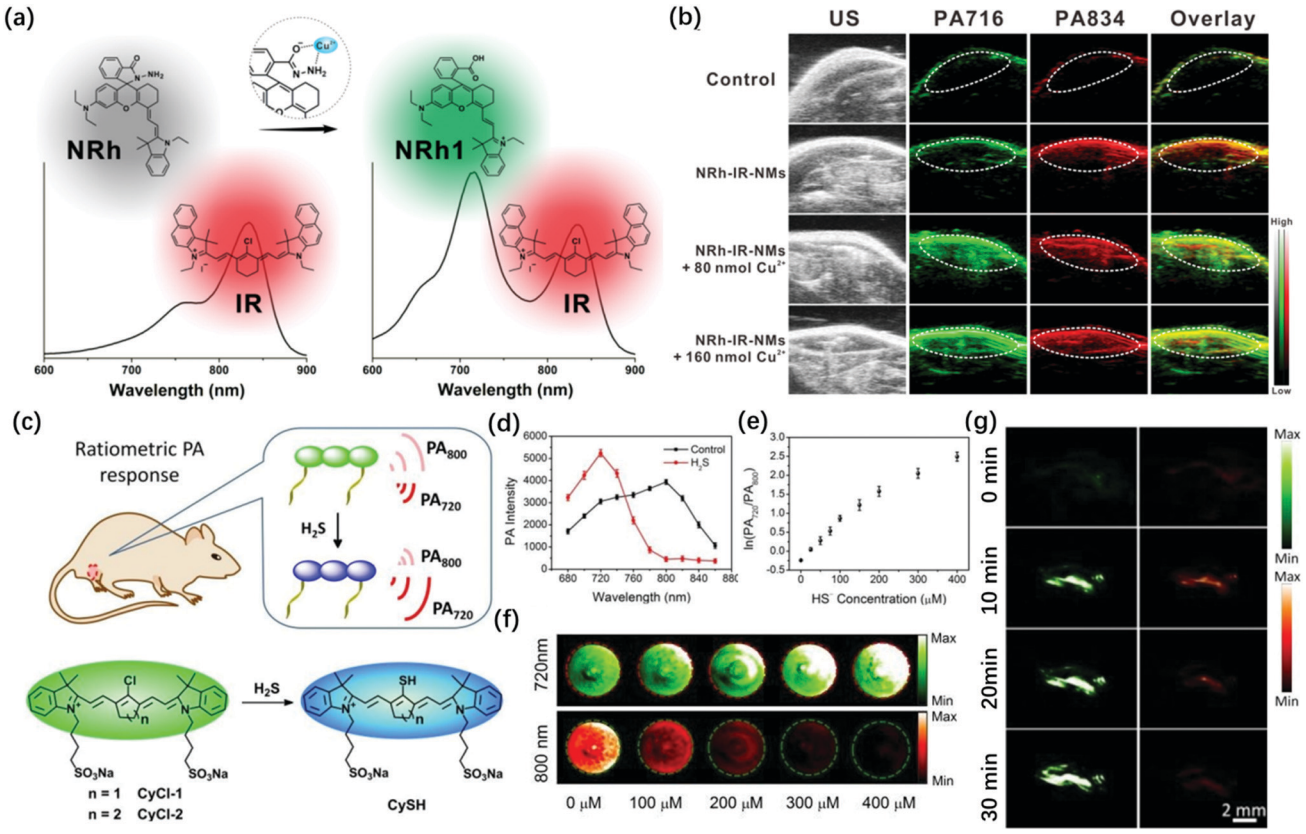

Fig. 3 (a) The structure and absorption spectra changes of the NRh-IR-NMs in the presence of Cu^{2+}. (b) PA images of living mice after subcutaneous administration of saline and NRh-IR-NMs solution with or without Cu^{2+}. Adapted from ref. 50. Copyright© 2018 American Chemical Society. (c) Structures of CyCl-1 or CyCl-2 and the proposed mechanism for H_2S detection. (d) PA spectra of CyCl-1 (50 μM) in PBS (pH 7.4) before (black line) and after (red line) incubation with 400 μM of HS^-. (e) The logarithmic value of PA720/PA800 as a function of HS^- concentration. (f) PA images of CyCl-1 solutionin the presence of different concentrations of HS^-, excitation at 800 nm (red) and 720 nm (green). (g) *In vivo* PA images of NaHS pretreated regions in the thigh of living mice before (0 min) and after injection of CyCl-1 for 2, 10, and 30 min. Adapted from ref. 51. Copyright© 2019 Royal Society of Chemistry.

Open Access Article. Published on 24 kovo 2021. Downloaded on 2026-01-19 22:31:07.
This article is licensed under a Creative Commons Attribution-NonCommercial 3.0 Unported Licence.

Tian *et al.* synthesized a series of iron(II) complexes.[54] Among them, S–Fe iron(II) complexes have superior photothermal conversion efficiency and excellent PA outcome both *in vitro* and *in vivo*. The good hydrophilic properties and less cytotoxicity furnished potential in photothermal therapy and non-invasive diagnosis. However, some cyanine and BODIPY dyes exhibit weak fluorescence signals due to ground state bleaching, which limits their biological applications. To solve this problem, Frenette *et al.* studied the photoacoustic properties of BODIPY, Cy3, $(MeOPh)_2$BODIPY, and curcuminBF_2 through optical and photoacoustic Z-scan spectroscopy. It was found that the photoacoustic emission of $(MeOPh)_2$BODIPY and curcuminBF_2 was stronger than that of the orignal BODIPY and Cy3. The reason for the enhanced PA emission may be attributed to the continuous absorption of the excited states and the rapid non-radiative decay of $S_n \rightarrow S_1$. This provided a theoretical basis for the design of BODIPY and curcumin skeleton dyes with enhanced PA signal.[55] Subsequently, in 2007, Frenette *et al.* conducted a detailed study on the influence of the structure of different donor–π–acceptor–π–donor curcumin on photoacoustic emission. Thereby, the author synthesized a series of curcuminBF_2 molecules by extending the conjugation of the aryl group on the donor and the functional design of the amino-terminal on the donor. The study found that at a low laser fluence of 15 mJ cm^{-2}, bis-carbazole curcuminoid (9) showed the strongest molar PA emission at 1.19×10^4 V M^{-1}. When the laser fluence was increased to 360 mJ cm^{-2}, the molar PA emission of bis-carbazole curcumin increased by 8.7 times, which was 4 times higher than that of the LA crystal violet dye (2.7 times). This result confirms the non-linear enhancement of its molar PA emission.[56]

Although the above-mentioned examples are successfully applied *in vitro* and *in vivo*, there is still some room for improving the wavelength of PAI probes. Generally speaking, PAI in the NIR-II window provides clear advantages over that in the conventional NIR-I window (700–1000 nm) for deeper tissue imaging as it provides higher maximum permissible exposures (MPEs) (*e.g.*, λ_{ex} at 800 nm is ~300 mW cm^{-2} and at 1064 nm is ~1000 mW cm^{-2} per laser pulse) and reduced light scattering in the tissues. In 2016, Lovell *et al.* synthesized a phosphorous phthalocyanine dye (P-Pc) with an absorption wavelength in the NIR-II window through commonly used surfactants. The photoacoustic signal generated by the probe could pass through 11.6 cm chicken breasts. It can also perform non-invasive photoacoustic imaging of mouse tumors and intestines. Besides, photoacoustic computed tomography (PACT) can easily detect the photoacoustic signal of P-Pc under the arm of a healthy adult.[57] In 2019, Li *et al.* combined the advantages of croconaine dyes A1090 whose large conjugated structure results in strong and sharp near-infrared absorption at 1090 nm and the advantages of J-aggregates than the dyes' absorption enhancement when encapsulated by DSPE-PEG_{2000} (Fig. 4a).[58] The PA signal of the J-aggregates probe at 900–1300 nm was significantly stronger than that of its monomer; thus, it can be used for PAI in the NIR-II region (Fig. 4b). This probe showed a better PAI effect in the mouse brain, which was consistent with the abnormal area obtained in the ultrasound image, with a lower background signal and higher contrast image at 1200 nm (Fig. 4c). In 2020, Hiroyuki *et al.* reported novel core-modification for controlling the molecular geometries of dioxohexaphyrin scaffolds (Fig. 4d).[59] The bis-metal complexes of dioxohexaphyrins exhibited superior PA spectral features. Meanwhile, Kim *et al.* reported that a nickel dithiolene-based polymeric nanoparticle (NiPNP) absorbed in the NIR-II region (Fig. 4e).[60] Thanks to the advantage of non-linear optics of NIR-II, it has made NiPNP more stable and deeper penetrability of bio-imaging (~3.4 cm) (Fig. 4f). Dong *et al.* synthesized the NIR-II photoacoustic probe Bodipy-Fe(III) NPs with H_2O_2 response through the coordination of Fe^{3+} with catechol, which can extend the absorption to 1300 nm for enhanced ligand-to-mental transfer (Fig. 4g).[61] Due to the high signal-to-background in NIR-II PAI, Bodipy-Fe(III) NPs showed high PAI quality (Fig. 4h).

2.2 Multi-functional photoacoustic probes

Compared with conventional NIR-I fluorescence imaging, photoacoustic imaging can overcome the shortcomings of NIR-I FL in terms of the penetration depth. However, PAI still has a challenge in tracking rapid biological processes because it needs time to carry out 3D volumetric images. Meanwhile, the high sensitivity, fast feedback, and precise disease boundary identification could provide a good supplement for PA imaging. Therefore, it is necessary to combine the advantages of photoacoustic imaging and NIR fluorescence imaging. Wang *et al.* successfully applied ICG for both FL and PA imaging.[62] The results showed that the dual-modality, when used together with ICG, had the potential to help map SLNs in axillary staging and to help evaluate tumor metastasis in patients with breast cancer. In 2017, Pu *et al.* reported the design and synthesis of an amphiphilic semiconducting oligomer (ASO) as a probe for photoacoustic and fluorescence imaging with improved stability and enhanced photoacoustic signal.[63] The semiconducting backbone served as the signal source that efficiently converts the photon energy into fluorescence and PA signals, while the PEG side chains provide water-solubility and shield the hydrophobic backbone to reduce non-specific interactions with plasma proteins. However, due to the difference in the penetration depth between PAI and NIR-I FL images, there were some problems in the accurate matching of these two imaging modalities. Thus, NIR-II FL imaging and PA imaging can address these issues because there have similar penetration depth. Although photoacoustic imaging has superior penetration depth, spatial resolution, and three-dimensional capabilities, which is good for providing preoperative volumetric images, however, the surface visualization of organs or tissues is not as good as fluorescence imaging because PAI has lower temporal resolution and sensitivity than NIR-II imaging (3 min *vs.* 100 ms). Therefore, NIR-II FL imaging has a clearer boundary profile than photoacoustic imaging. Hence, it is necessary to combine the advantages of photoacoustic imaging and NIR-II fluorescence imaging. Based on this concept, Chen *et al.* recently modified the existing NIR-II fluorescence molecular dye CH1055 by adjusting its substituents to form a lipophilic molecule,

 © 2021 The Author(s). Published by the Royal Society of Chemistry

Open Access Article. Published on 24 kovo 2021. Downloaded on 2026-01-19 22:31:07.
This article is licensed under a Creative Commons Attribution-NonCommercial 3.0 Unported Licence.

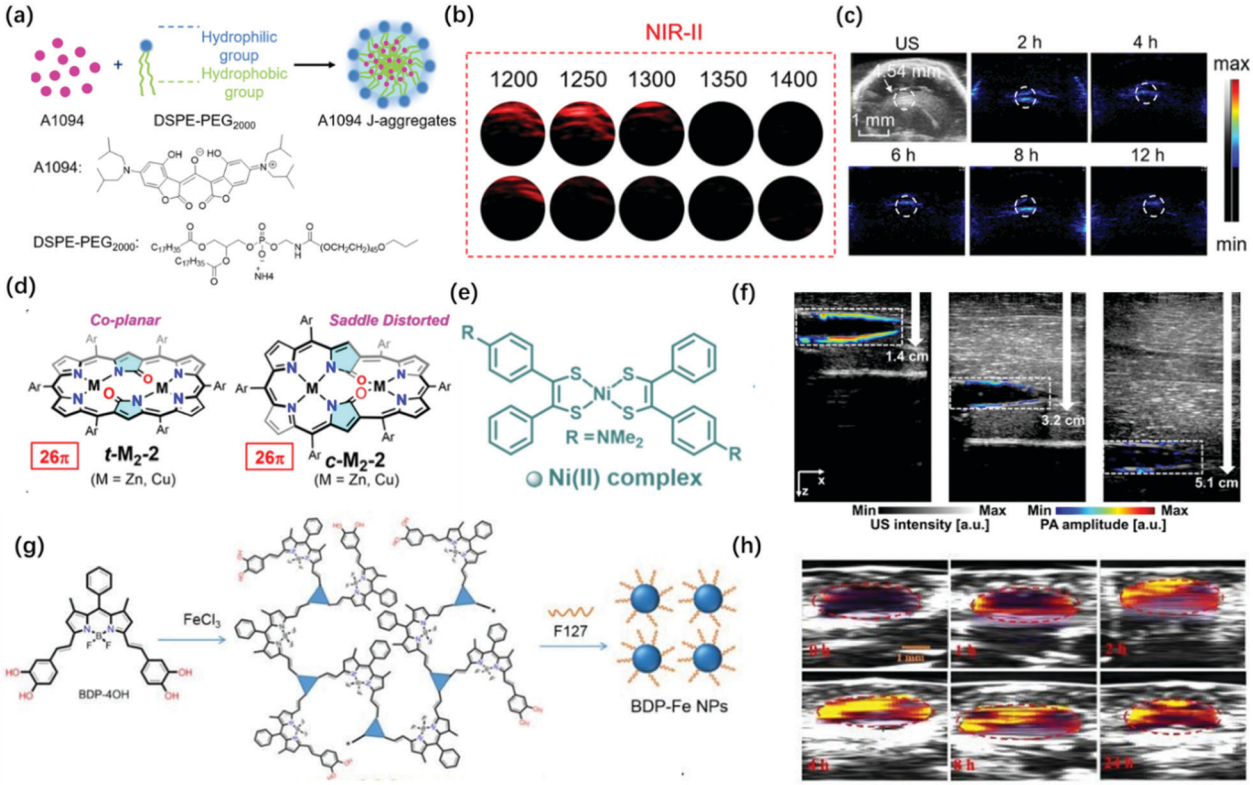

Fig. 4 (a) Preparation of A1094 J-aggregate nanomicelles through self-assembly. (b) PA intensity of the A1094 J-aggregates and the A1094 monomer phantoms at different wavelengths. (c) PA images of mouse brain glioma at different time points *in vivo* at 1200 nm. Adapted from ref. 58. Copyright© 2019 American Chemical Society. (d) Redox-interconvertible hexaphyrins containing doubly N-fused congeners with different molecular symmetries can serve as functional and tunable NIR-II PA dyes. Adapted from ref. 59. Copyright© 2020 American Chemical Society. (e) Depiction for the preparation of NiPNP. (f) PA/US overlaid images of the tube filled with NiPNP at different depths prepared with chicken breast tissues. Adapted from ref. 60. Copyright© 2020 Royal Society of Chemistry. (g) Synthetic route and schematic diagram of BDP-FeNPs. (h) PA images of BDP-FeNPs injected mice at a different time under 1100 nm laser irradiation; the tumor region is encircled. Adapted from ref. 61. Copyright© 2020 Royal Society of Chemistry.

which was named CH1000.[64] CH1000 easily formed water-soluble nanoparticles through the DSPE-PEG encapsulation, which demonstrated both photoacoustic and fluorescence properties, and it then conjugated with antibodies (EGFR affibody, targeting ligand) to improve the biological compatibility and enhance the photoacoustic and fluorescence signals in the tumor region by the targeting effect (Fig. 5a). The *in vivo* imaging results indicated that the Affibody-DAP had excellent photoacoustic and fluorescence signals in FTC-133 subcutaneous mouse model imaging and could selectively target EGFR-positive tumor (Fig. 5b).

Multi-modal imaging combined with photoacoustic, fluorescence, MRI, or PET to guide disease treatment has naturally become the mainstream.[65] Firstly, as mentioned above, multi-mode imaging has excellent practical applications in preclinical and clinical practice. Secondly, the designed all-in-one probes for PA/FL dual-modal imaging could greatly reduce the interference between each modality. Last but not least, the multi-mode imaging probe can more precisely guide the treatment of diseases. Due to the unique delocalized π-electron framework, porphyrin-related molecules can not only be used for fluorescence and photoacoustic imaging but can also chelate metal ions for MRI or PET imaging. Also, combining the inherent photodynamic and photothermal properties of this type of structure can realize multimodal imaging-guided precise treatment.[66–69] Lovell *et al.* used the hydrophobicity of naphthalocyanine dyes to prepare frozen micelles with absorption wavelengths greater than 1000 nm. The probe could not only withstand the harsh conditions of the stomach and intestines while avoiding systemic absorption but also provided high-resolution imaging of the intestines through real-time US/PA signals. Subsequently, the author loaded ^{64}Cu in Nanonap to prepare a multimodal probe for whole-body PET imaging of mouses. It can be used to track the movement of nanoparticles in the gastrointestinal tract. Although multimodal imaging can accurately locate the lesion, it has not achieved the treatment of the disease.[70] To solve this problem, Ntziachristos *et al.* introduced silicon into the center of naphthalocyanine to prepare a photoacoustic probe that has strong absorption in the near-infrared region and can generate singlet oxygen. The probe can identify the location of tumors in mice through photoacoustic imaging. Through multispectral photoacoustic tomography technology (MSOT), the probe can trigger the generation of reactive oxygen species at the highest energy setting for photodynamic therapy. Besides, MSOT can monitor the rate of active oxygen generation by evaluating the content of naphthalocyanine present in the image.[71] In 2011, Zheng *et al.* developed a multifunctional photoacoustic probe assembled by

Open Access Article. Published on 24 kovo 2021. Downloaded on 2026-01-19 22:31:07.
This article is licensed under a Creative Commons Attribution-NonCommercial 3.0 Unported Licence.

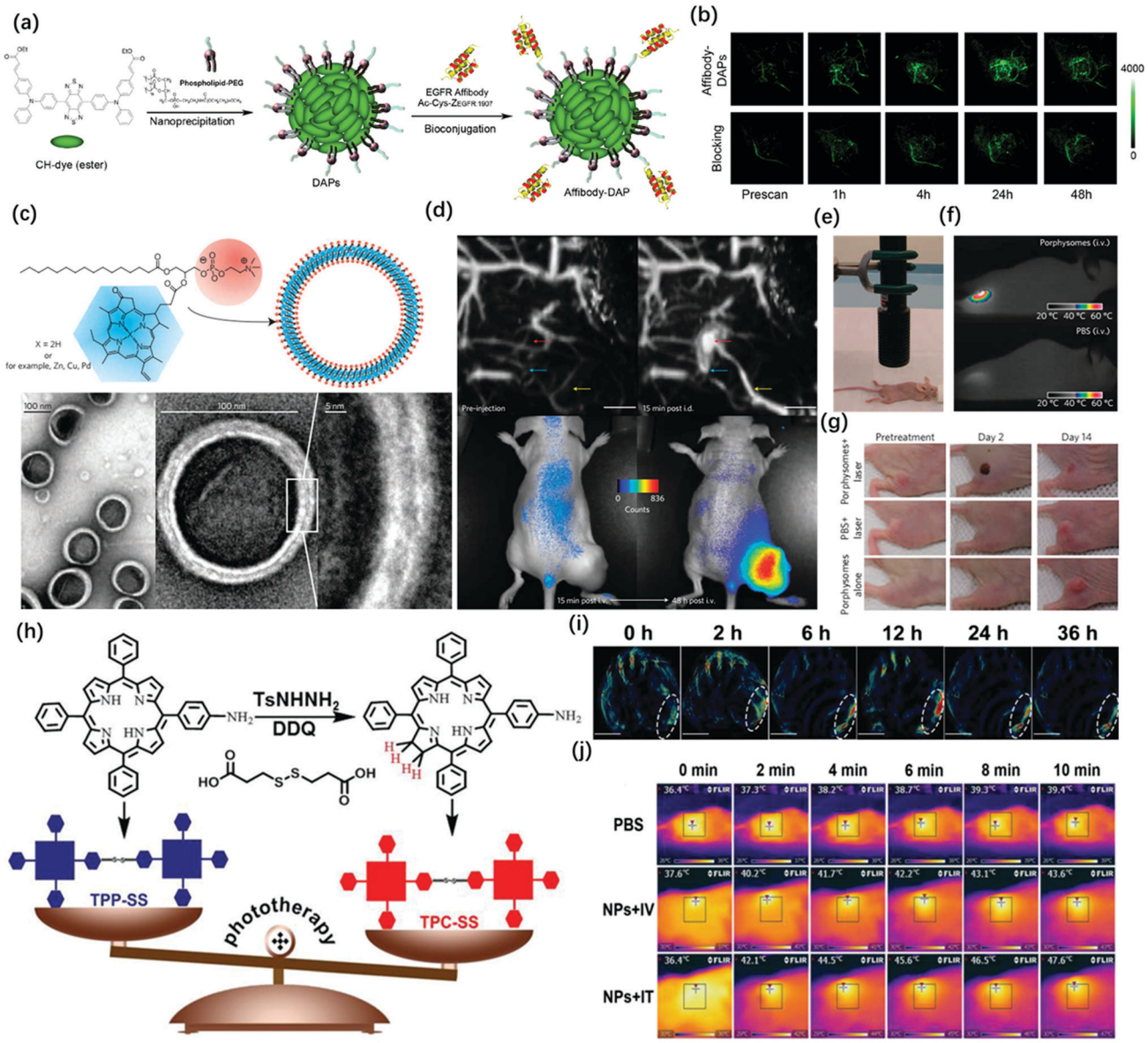

Fig. 5 (a) Schematic illustration of the preparation of Affibody-DAPs. (b) Coronal views of 3D volume rendering of photoacoustic images of FTC-133 tumors were acquired immediately after fluorescence imaging at the predetermined time intervals. Adapted from ref. 61. Copyright© 2017 American Chemical Society. (c) Schematic representation of a pyropheophorbide–lipidporphysome (above). The phospholipid head group (red) and porphyrin (blue) are highlighted in the subunit (left) and the assembled nanovesicle (right). Electron micrographs of negatively stained porphysomes (5% PEG–lipid, 95% pyropheophorbide-lipid) (bottom). (d) Dual modality for photoacoustic contrast and activatable fluorescence. Top, lymphatic mapping. Rats were imaged using photoacoustic tomography before and after intradermal (i.d.) injection of porphysomes (2.3 pmol). Secondary lymph vessels (cyan), lymph node (red), inflowing lymph vessel (yellow), and 5 mm scale bar are indicated. Bottom, fluorescence activation after i.v. injection of porphysomes (7.5 pmol) in a KB xenograft-bearing mouse. (e) Photothermal therapy set-up showing the laser and the tumor-bearing mouse. (f) Representative thermal response in KB tumor-bearing mice injected intravenously 24 h before with 42 mg kg^{-1} porphysomes or PBS. Thermal image was obtained after 60 s of laser irradiation (1 : 9 W cm^{-2}). (g) Photographs showing the therapeutic response to photothermal therapy using porphysomes. Adapted from ref. 72. Copyright© 2011 Springer Nature. (h) Schematic illustrations of the synthetic procedures of TPP-SS and TPC-SS. (i) *In vivo* PA imaging of tumor tissue before and after tail vein injection of TPC-SS NPs upon 680 nm laser irradiation at different time points (0, 2, 6, 12, 24, and 36 h). (j) Infrared thermal images of U14 tumor-bearing mice injected with PBS and TPC-SS NPs by intravenous and intratumor injection, respectively, exposed to 635 nm laser at a power density of 360 and 240 J cm^{-1} recorded at different time intervals, respectively. Adapted from ref. 73. Copyright© 2018 John Wiley and Sons.

porphyrin-lipid conjugates, which exhibits good PA and NIR-I FI characteristics, and can image lymph nodes and tumors in rodent models (Fig. 5c and d). Because the probe exhibits a good PTT effect in the form of nanovesicles, it could be used for PA/FL-guided photothermal therapy (Fig. 5e and f) and can completely ablate mouse subcutaneous tumors during 14 day treatment (Fig. 5g).[72] In 2018, Xie *et al.* synthesized chlorin dimer (TPC-SS) nanoparticles using an autonomous assembly strategy (Fig. 5h). Compared with porphyrin monomer, the probe exhibits higher molar absorbance; thus, it had enhanced

 © 2021 The Author(s). Published by the Royal Society of Chemistry

Open Access Article. Published on 24 kovo 2021. Downloaded on 2026-01-19 22:31:07.
This article is licensed under a Creative Commons Attribution-NonCommercial 3.0 Unported Licence.

photodynamic and photothermal effects when irradiated by a laser. *In vitro* experiments showed that the photoacoustic signal increases with the increase in the concentration of TPCSS NPs (Fig. 5i). Tumor growth on mice models was inhibited by photothermal and photodynamic therapy guided by photoacoustic imaging (Fig. 5j).[73]

More recently, Sun *et al.* designed a single NIR-II molecular dye SYL and realized PA/FL dual-mode imaging-guided breast cancer photothermal therapy.[29] They rendered SYL better fluorescence performance by extending the electron-density and molar extinction coefficient due to the addition of a secondary electron donor (diphenylamine) to the molecular scaffold (Fig. 6a). This probe had an obvious inhibitory effect on breast tumor growth under laser irradiation (Fig. 6b). The *in vivo* studies confirmed that SYL NPs showed bright NIR-II fluorescence and PA signals in the tumor region (Fig. 6c). At the same time, Sun *et al.* reported a molecular dye named SY1080, which loaded the heavy atom selenium from previous NIR-II dye H1 to reduce the energy gap; thus, the emission wavelength can be red-shifted to improve the performance of photoacoustic and fluorescence imaging.[30] SY1080 was further modified with DSPE-PEG to form a nanoparticle-based NIR-II probe, possessing high biocompatibility, stability, and tumor-targeting capability. Besides photothermal therapy, chemotherapy is still the basic and most important approach for cancer treatments in clinical practice because of its high antitumor efficiency.[74] However, the lack of precise imaging guidance for therapeutic procedures is the challenge that chemists have to face.[75] Besides, a single chemotherapy also cannot simultaneously balance the needs for efficiency and safety as well as non-specific tumor targeting and systemic toxicity. In 2019, Stang and Sun synthesized a multifunctional photoacoustic imaging probe by both loading macrocyclic platinum drugs and NIR-II fluorescent dyes on the theranostic platform containing melanin dots (Fig. 6d). The probe had good solubility, biocompatibility and stability *in vivo*, and realized the precise treatment of tumors by NIR-II FL/PA dual-modal imaging-guided chemotherapy and photothermal therapy (Fig. 6e and f).[28] In addition, photoacoustic imaging can be used in combination with other approaches for therapy, such as photodynamic therapy or gene therapy, so as to

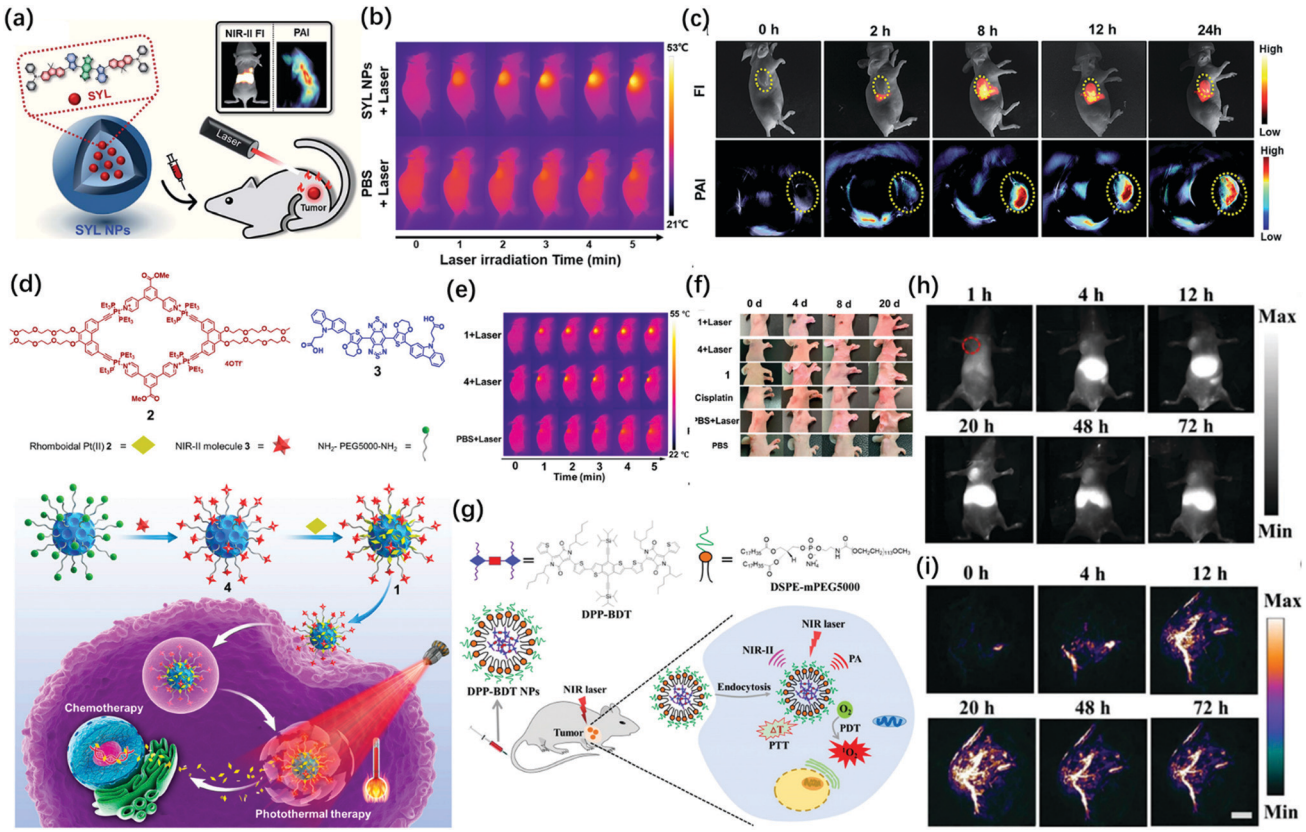

Fig. 6 (a) Schematic illustration of the preparation of SYL NPs, as well as their multifunctional applications in NIR-II/PA dual-modal imaging and photothermal therapy. (b) IR thermal images of 4T-1 bearing mice injected with SYL NPs and PBS under irradiation (808 nm, 1 W cm^{-2}). (c) *In vivo* NIR-II fluorescence (100 ms, LP 1000, 82 mW cm^{-2}) and PA images of 4T1 tumor-bearing mice at 0, 2, 8, 12, and 24 h after tail vein injection of SYL NPs. Yellow circles indicate tumor sites. Adapted from ref. 29. Copyright© 2019 Royal Society of Chemistry. (d) Structures of discrete Pt(II) metallacycle 2 and NIR-II molecular dye 3. Schematic diagram of nano-agent 1 in chemo-photothermal synergistic therapy. (e) IR thermal images of mice treated with PBS, nano-agent 1, and 4 dots with laser irradiation. (f) Temperature changes ($T-T_0$) of mice treated with PBS, nano-agent 1, and 4 during laser irradiation at various times. Adapted from ref. 28. Copyright© 2019 National Academy of Science. (g) Schematic illustration of DPP-BDTNPs for NIR-II fluorescence/PA imaging and simultaneous PDT/PTT combination therapy. (h) NIR-II fluorescence imaging of DPP-BDTNPs at different time points and (i) PA imaging. Adapted from ref. 76. Copyright© 2019 Royal Society of Chemistry.

Open Access Article. Published on 24 kovo 2021. Downloaded on 2026-01-19 22:31:07.
This article is licensed under a Creative Commons Attribution-NonCommercial 3.0 Unported Licence.

improve the efficiency of treatment. For example, Fan *et al.* in 2019 successively developed two types of probes integrated for diagnosis and treatment (Fig. 6g).[76] DPP-BDT NPs as an all-in-one probe was applied for dual-mode imaging-guided combined photothermal and photodynamic therapy (Fig. 6h and i). Furthermore, the modified P(DPP-BT/DOX) NPs added the chemotherapy drug DOX and enhanced the biocompatibility through amphiphilic lecithin. These all-in-one probes were simultaneously applied in NIR-II FL/PA imaging and photodynamic combined with photothermal and chemotherapy. It has unlimited potential in clinical medicine.

3. Activatable photoacoustic probes

Existing research shows that many biologically relevant species play important roles in various physiological processes, such as reactive oxygen species (ROS),[77,78] metal ions,[79,80] and enzymes.[81,82] Abnormal levels of these species are associated with many diseases. In addition, hypoxia[83,84] and acidic pH[85,86] are common pathological microenvironments. Therefore, monitoring the changes in hypoxia, pH, or the levels of various biomarkers in organisms is of great significance for the diagnosis and prognosis of related diseases.

"Always on" probes generally detect biomarkers based on the difference in the signal intensity caused by the discrepancy in concentration between diseased tissue and normal tissue. The signal strength of these probes remains "on" regardless of whether they are successfully anchored to the targets or not, which greatly reduces the sensitivity and specificity of detection.[87,88] In order to overcome the shortcomings of the current "always on" PAI probes, activatable PAI probes were developed. The signals of such probes at non-target tissues are in the "off" state and they will only be activated to send out signals when there is a biomarker or molecular event of interest.[89–92] Compared with "always on" probes, activatable PAI probes can obtain a higher target-to-background ratio (TBR) and lower limit of detection (LOD), which further improves the specificity and sensitivity of early disease diagnosis. Therefore, the following will mainly discuss the research progress of activatable PA probes based on organic small molecule dyes.

3.1 Reactive oxygen species

Reactive oxygen species are a set of short-lived species, mainly including superoxide ($O_2^{\bullet-}$), hydrogen peroxide (H_2O_2), peroxynitrite ($ONOO^-$), hypochlorite (OCl^-), nitric oxide (NO), and hydroxyl radicals ($^{\bullet}OH$). Studies have shown that oxidative stress can induce intracellular redox imbalance and biomolecular damage, leading to the occurrence of many diseases, including cancer and cardiovascular disease.[93,94] Although ROS has damaging effects, it also has positive effects. For example, photodynamic and sonodynamic therapy based on an appropriate increase in the reactive oxygen species can induce cell senescence and apoptosis, thereby showing anti-tumor functions. Therefore, the design of ROS activatable PA probes are of great value for the study of related pathological events.

$O_2^{\bullet-}$, as an important ROS, is involved in inflammatory disorders as well as in cancer.[95] Therefore, the imaging of unstable $O_2^{\bullet-}$ is beneficial for the study of diverse related pathological processes. Banala *et al.* reported a novel approach to capture the triggers by the non-covalent complexation of the response molecules for the first time and synthesized superoxide sensing probes for PA imaging based on porphyrin, oxoporphyrinogen, and metalloporphodimethene dyes including 1-2H, 1-Ni, 1-Zn, 2(OxP), 3-Ni, and 3-Zn (Fig. 7a).[96] The complexation of the probes and $O_2^{\bullet-}$ or F^- would cause an enhancement in the PA signal, accompanied by a red-shift in the spectrum. Unlike the probes containing cleavable groups, which exhibit continuous consumption of the substrates, these probes were almost time-independent. Therefore, the non-covalent complexation strategy could achieve a higher signal-to-noise ratio (SNR). By screening the stability, biocompatibility, red-shift in $\lambda_{PA_{max}}$, and gain in the PA signal for $O_2^{\bullet-}$ of these probes, it has been found that oxoporphyrinogen 2 exhibited excellent optical properties in response to $O_2^{\bullet-}$ with a 9.6-fold stronger PA signal and a red-shift of 89 nm (PA_{max}: 745 nm) (Fig. 7b). Moreover, probe 2 had high biocompatibility and stability after $O_2^{\bullet-}$ activation. Therefore, it was considered that 2 has great potential for imaging $O_2^{\bullet-}$ *in vivo*.

$ONOO^-$ is another kind of reactive oxygen molecule, which is generated by the reaction of endogenous NO.[97] $ONOO^-$ can nitrate biological macromolecules and destroy their biological functions, leading to mitochondrial dysfunction and cell apoptosis.[98,99] In addition, $ONOO^-$ is also closely related to tumor immunosuppression.[100] Therefore, the real-time imaging of $ONOO^-$ in tumors is one of the keys to understand the pathological function of $ONOO^-$ and develop innovative tumor therapy. Pu's group reported the first PA/FL dual-modal smart molecular probe ($CySO_3CF_3$) for the detection of the endogenous $ONOO^-$ in a living system.[101] In the presence of $ONOO^-$, the non-fluorescent $CySO_3CF_3$ in the "caged" state was converted into the uncaged molecule $CySO_3OH$ through a series of cascade oxidation-elimination reactions and the fluorescence was converted from "OFF" to "ON" with ~59-fold increase due to the enhancement of the electron-donating ability of the oxygen atom in the probe. The fluorescence and photoacoustic of CyOH activated by $ONOO^-$ enabled highly specific NIR-FL/PA dual-modal imaging of $ONOO^-$ *in vivo*. The previous study has demonstrated that ROS are effective biomarkers of acute kidney injury (AKI, drug-caused nephrotoxicity is quite common in-hospital acute kidney injury) at the incipient stage.[102] Zhang *et al.* designed a mitochondria-targeted (the initial and primary source of endogenous $ONOO^-$) NIR-FL/PA dual-modal probe SiRho-HD for imaging the fluctuation of $ONOO^-$ in cisplatin-induced AKI.[102] The probe was based on Foster resonance energy transfer (FRET), which was constructed by combining HD dye analogue (energy receptors, capable of oxidative cleavage by $ONOO^-$, and stable in the presence of other oxidants or nucleophiles) with another near-infrared dye, Si-rhodamine (energy receptors, with good water solubility for

 © 2021 The Author(s). Published by the Royal Society of Chemistry

Open Access Article. Published on 24 kovo 2021. Downloaded on 2026-01-19 22:31:07.
This article is licensed under a Creative Commons Attribution-NonCommercial 3.0 Unported Licence.

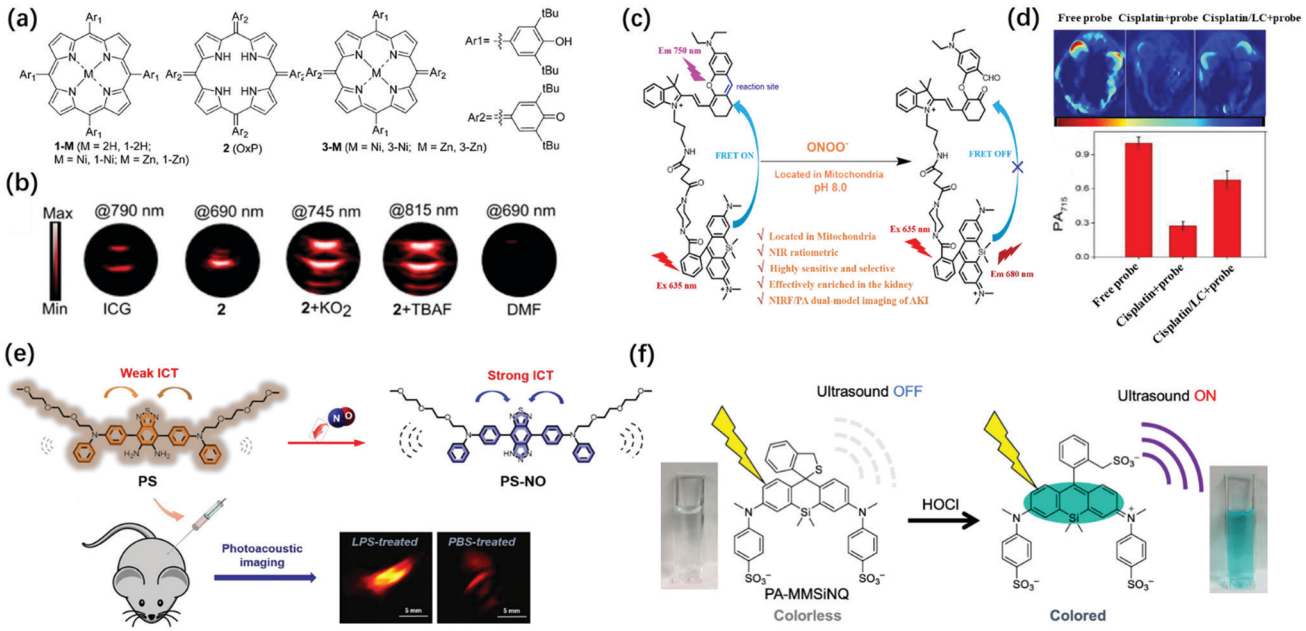

Fig. 7 (a) Schematic Illustration for the construction of 1-2H, 1-Ni, 1-Zn, 2 (OxP), 3-Ni, and 3-Zn. (b) PA images of tube phantoms containing ICG, 2, 2 + KO_2 (which was used to obtain K^- that complexed with 18-crown-6 to produce "free" $O_2^{\bullet -}$), and 2 + TBAF (tetrabutylammoniumfluoride, which was used to obtain F^-) for excitation at their PAmax, and DMF as the control. Adapted from ref. 96. Copyright© 2019 Royal Society of Chemistry. (c) The transformation response of PS probe after reaction with endogenous NO. (d) Design of SiRho-HD and its response mechanism to $ONOO^-$. Adapted from ref. 102. Copyright© 2020 Royal Society of Chemistry. (e) PA images and average intensity from the kidneys in the living mice after intraperitoneally pre-injecting with normal saline, cisplatin, or L-carnitine + cisplatin for 48 h, then intravenous injection of SiRho-HD for 1.5 h. Adapted from ref. 105. Copyright© 2018 Elsevier. (f) Structure of PA-MMSiNQ and its response mechanism to HOCl. Adapted from ref. 110. Copyright© 2019 American Chemical Society.

renal targeting, excellent photostability, and fluorescence brightness) through a short piperazine-flexible carbon chain (Fig. 7c). The ratio of fluorescence intensity between 680 and 750 nm under 635 nm laser excitation showed about 19-fold enhancement after SiRho-HD was $ONOO^-$ activated, while the PA signal intensity at 715 nm showed a 3.9-fold decrease. SiRho-HD with high renal targeting ability has been successfully applied *via* intravenous injection for the highly sensitive and specific NIR-FL/PA dual-modal imaging of $ONOO^-$ in cisplatin-induced AKI in a murine model (Fig. 7d). Therefore, SiRho-HD was expected to reveal the role of $ONOO^-$ in drug-induced AKI. NO is also an important active oxygen molecule. Abnormal NO can cause lysosomal storage disorders, neurodegenerative damage, and many other diseases.[103,104] Zhang *et al.* designed a novel off–on photoacoustic and on–off fluorescent probe PS with high sensitivity and selectivity to effectively detect the distribution and content of NO in cells and complex biological systems (Fig. 7e).[105] The NO probe PS had two diphenylamine groups (which conjugated an oligoether group respectively to increase the amphipathic of the probe for further biological applications) as electron donors and benzothiadiazole as the electron acceptor to obtain a typical donor–acceptor–donor (D–A–D) structure. The aromatic diamine of the acceptor moiety could react with NO under aerobic conditions, the electron-withdrawing ability of the receptor moiety was enhanced as PS becomes a triazole structure (PS-NO), leading to stronger intramolecular charge transfer (ICT), accompanied by fluorescence quenching and PA signal amplification. The PS probe was successfully applied for the fluorescence imaging of endogenous NO in RAW264.7 cells and the PA imaging of lipopolysaccharide-induced inflammation mouse models.

Unlike $ONOO^-$, HClO is a weakly acidic reactive oxygen species that plays an important role in the human immune system, helping to destroy invading bacteria and pathogens.[106,107] However, excessive HClO can cause oxidative stress, leading to tissue damage, cardiovascular diseases, cancer, and kidney diseases.[108,109] Given the biological importance of HClO, monitoring the change and dynamic distribution of hypochlorous acid concentration in living systems has become an important topic in biomedicine. Urano *et al.* explored a new strategy to enhance the conversion efficiency from absorbed light to the ultrasound of dye molecules, which was to reduce the fluorescence quantum yield by introducing aromatic rings on the N atoms at the 3,6-positions of the xanthene moiety of rhodamine derivatives to ensure that the light energy of the dye was converted to the PA signal to the maximum extent.[110] Based on this strategy, a novel near-infrared-absorbing, non-fluorescent rhodamine dye 2-Me wsSiNQ660, subsequently applied 2-Me wsSiNQ660 to a HOCl activatable PA probe in combination with the spirocyclization off/on switching strategy and successfully performed 3D PA imaging of HClO in mouse subcutis (Fig. 7f). This 2-Me wsSiNQ660 scaffold had great potential to develop a wide range of activatable PA probes, such as enzymes, metal ions, and pH.

Open Access Article. Published on 24 kovo 2021. Downloaded on 2026-01-19 22:31:07.
This article is licensed under a Creative Commons Attribution-NonCommercial 3.0 Unported Licence.

3.2 Reactive sulfur species

Similar to reactive oxygen species, reactive sulfur species (RSS) are also an important class of biologically active molecules in organisms. Reactive sulfur species mainly include three biological thiols (cysteine, homocysteine, and glutathione) and hydrogen sulfide.[111,112] As an antioxidant and signaling agent for tissues, RSS is widely involved in many physiological reactions to maintain cell health in the body, including the liver, brain, and circulatory system. Further, its concentration imbalance in the cells is closely related to the occurrence of certain human diseases.[113,114] Therefore, real-time monitoring of the concentration of these biologically active molecules in the body is of great significance for related physiological and pathological research. At present, the activatable PA probe has been successfully applied to RSS photoacoustic imaging *in vivo* based on its deep tissue penetration and high spatial resolution.

Hydrogen sulfide (H_2S), as the third signaling molecule, plays an important role in maintaining the normal function of the cardiovascular and nervous systems.[115,116] Zhao *et al.* developed the first example of activatable photoacoustic probe Si@BODPA for the real-time imaging of endogenous H_2S.[117] Si@BODPA has excellent water solubility, outstanding biocompatibility, and extremely fast responsiveness since the probe was composed by encapsulating semi-cyanine-BODIPY hybrid dyes (BODPA) into the hydrophobic interior of core–shell silica nanocomposites (Fig. 8a). The nanoprobe initially entered the cells through endocytosis. In the presence of H_2S, the hydrophilic core–shell component of the probe transferred H_2S from the water to the polar interior and then rapidly underwent thiol-halogen nucleophilic substitution and triggered a high NIR absorption at about 780 nm, ultimately leading to the strong PA signal output. In addition, the probe showed a highly selective response to H_2S, with a detection limit of 53 nM. Based on the excellent properties of Si@BODPA, the probe had been used to image H_2S in an HCT116 (human colon cancer cells) tumor-bearing mouse model, thereby successfully verifying the promotion of cystathionine-β-synthase (CBS) upregulation on the increase in H_2S levels.

As the most abundant biological thiol (1–10 mM) in cells, glutathione (GSH) can regulate many physiological processes including cell redox activity, intracellular signal transduction, and gene regulation.[118,119] It is worth noting that GSH can protect cells from DNA and RNA damage caused by oxidative stress by capturing free radicals, thereby maintaining redox homeostasis in the body. Tang *et al.* developed a GSH/H_2O_2 redox couple-responsive BSA-Cy-Mito nanoprobe for the PA imaging of the redox state and the accurate assessment of the activity and vulnerability of plaque inflammation by introducing the self-assembly of bovine serum albumin (BSA) with two near-infrared fluorescence probes, Cy-3-NO_2 for GSH and Mito-NIRHP for H_2O_2 (Fig. 8b).[120] The introduction of BSA endowed the nanoprobe with good biocompatibility, long blood circulation time, and high plaque accumulation, and did not affect the specific response of the nanoprobe to GSH and H_2O_2. In the presence of GSH and H_2O_2, BSA-Cy-Mito exhibits strongly dependent

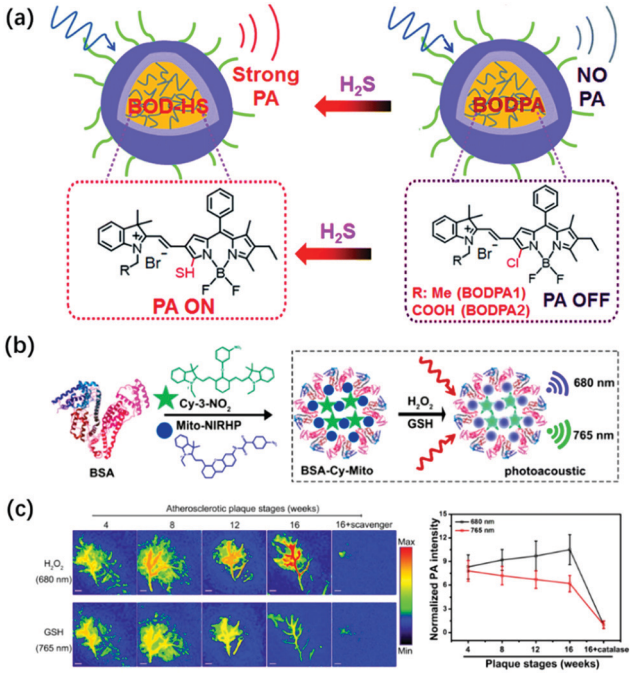

Fig. 8 (a) Structures of activatable photoacoustic probes Si@BODPA and illustration of Si@BODPA for the PA imaging of H_2S. Adapted from ref. 117. Copyright© 2017 Royal Society of Chemistry. (b) Design of GSH/H_2O_2-responsive BSA-Cy-Mito nanoprobe and its response mechanism to the redox state. (c) Representative PA imaging and semi-quantitative intensity of abdominal aortas of plaque-bearing ApoE$^{-/-}$ mice at different stages (4, 8, 12, and 16 weeks on a high-fat diet) injecting intravenously with BSA-Cy-Mito nanoprobe or pretreated with the scavenger. Adapted from ref. 120. Copyright© 2019 American Chemical Society.

absorbance at 765 nm and 680 nm, respectively, which enabled simultaneous the photoacoustic detection of GSH/H_2O_2 with high specificity and sensitivity with a detection limit of 0.9/0.5 μM. The nanoprobe had been successfully applied for the *ex vivo* PA imaging of inflammation in macrophages activated by oxidized low-density lipoprotein and *in vivo* accurate detection of vulnerable plaque in apolipoprotein E-deficiency (ApoE$^{-/-}$) mice (Fig. 8c). Thus, the probe had the potential to distinguish rupture-prone plaques from stable ones at an early stage, thereby helping in the implementation of successful prevention and treatment strategies.

Another important thiol in the organism is cysteine (Cys). Abnormal Cys concentration can lead to a variety of complex diseases, such as hair and skin damage, muscle weakness, and liver damage.[121,122] Current studies have shown that the synthesis of GSH in the lungs of patients with pulmonary fibrosis is limited but it has not been discovered whether this phenomenon is caused by the low level of raw material-Cys in the body.[123] To explore the reasons for the low level of GSH in pulmonary fibrosis, Tang *et al.* designed and synthesized a NIR-FL/PA dual-mode probe CCYS to detect the Cys level in the lungs of PF mice.[124] It found that the fluorescence and photoacoustic signals of Cys in the lungs of PF mice were significantly higher by comparing the Cys levels in healthy mice and mice with common pneumonia, which proved that limited GSH synthesis in pulmonary fibrosis

 © 2021 The Author(s). Published by the Royal Society of Chemistry

Open Access Article. Published on 24 kovo 2021. Downloaded on 2026-01-19 22:31:07.
This article is licensed under a Creative Commons Attribution-NonCommercial 3.0 Unported Licence.

was not caused by low Cys content. Further studies had found that the low activity of glutamyl cysteine ligase involved in the synthesis of GSH might be the cause of the low rate of GSH synthesis in pulmonary fibrosis. In addition, the experimental results of Cys over-expression in PF mice also provided a possible research direction for the early distinction between pulmonary fibrosis and common pneumonia.

3.3 Enzymes

Enzymes are one of the necessary conditions for major life activities. The growth, development, reproduction, heredity, movement, nerve conduction, and other life activities of organisms are closely related to the catalytic process of enzymes. At the same time, enzymes are also important biomarkers for certain pathological conditions, and their activity and concentration in the body or serum are generally regarded as important signal parameters for disease diagnosis.[125,126] Therefore, researchers have developed a series of probes for the imaging of various enzymes in living bodies. Among them, photoacoustic probes have shown great potential in enzyme detection based on their advantages of high spatial resolution and deep penetration depth.

The caspase family plays an extremely vital role in mediating cell apoptosis. Among them, caspase-3 is the only one that has been thoroughly studied so far. As a key executive molecule, caspase-3 is the main downstream effector caspase that cleaves the majority of the cellular substrates in apoptotic cells and functions in many pathways of apoptosis signal transduction.[127,128] Ye *et al.* developed an activatable photoacoustic probe 1-RGD based on the dual response of caspase-3 and GSH to detect the activity of caspase-3 in living organisms.[129] The probe connected CHQ as a pre-clickable site and modified the D cysteine residue with DEVD and disulfide bonds to serve as recognition sites for caspase-3 and GSH at the other end. In the apoptotic tumor microenvironment induced by chemotherapy, after the probe interacted with overproduced GSH and active caspase-3, the exposed free D-Cys condensed with the cyano of CHQ to form cyclized product 1-cycl and the self-assembly occurred (Fig. 9a). The fluorescence of the additional dye (ICG) undergoes aggregation-caused quenching (ACQ) after aggregation so that a strong PA signal was observed. 1-RGD had been successfully used for high-resolution 3D imaging of the spatial distribution of caspase-3 in apoptotic tumor tissues (Fig. 9b) and had great potential for the early monitoring of the efficacy of chemotherapy drugs on the tumors.

Hypoxia is a common pathological condition. When the oxygen supply in the cells is sufficient, the excessive expression

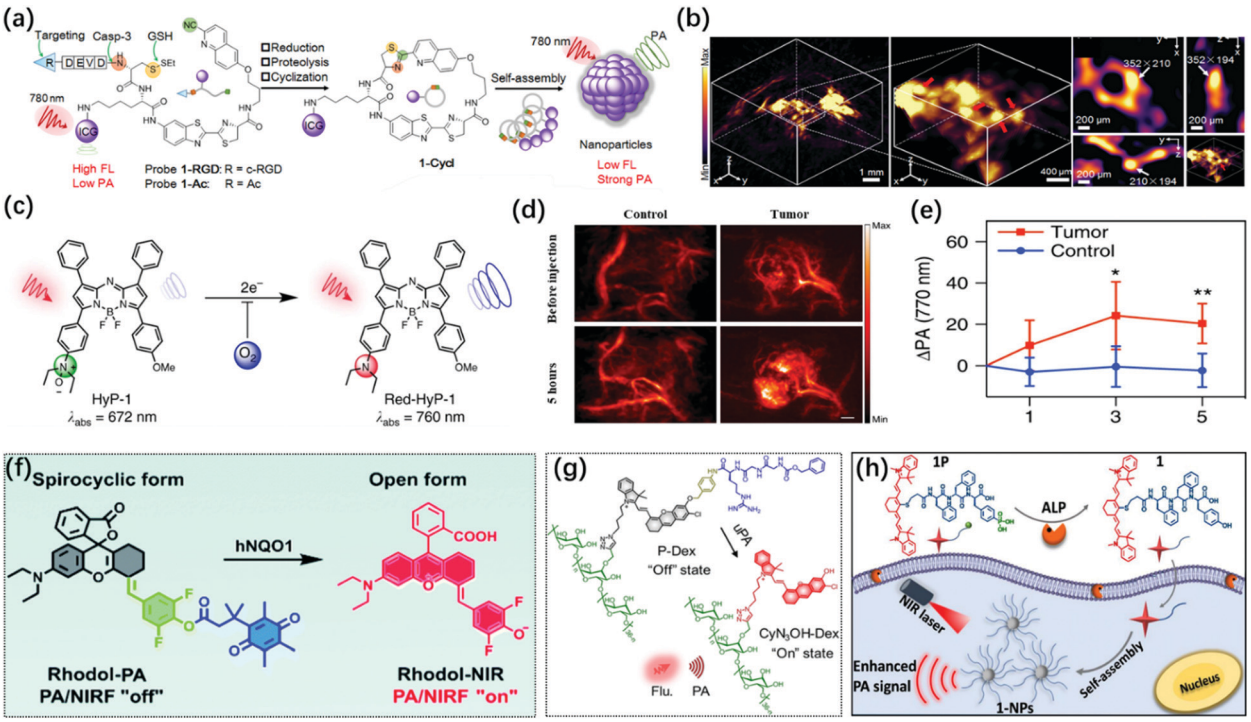

Fig. 9 (a) Construction of the PA probe (1-RGD and 1-Ac) and its response mechanism to caspase-3 *via* macrocyclization and self-assembly. (b) 3D Reconstruction PA image of apoptotic tumor (left) and 3D-slice in tumor tissues (right) in DOX-treated mice at 10 h after injection of 1-RGD. Red arrows showed the views of representative individual apoptotic region within the tumor tissues. White arrows show the same apoptotic region in the *xy*, *xz*, and *yz* panels. Adapted from ref. 129. Copyright© 2019 John Wiley and Sons. (c) Chemical structure of hypoxia-response probe HyP-1. (d) PA images of the tumor-bearing and control flank before and 5 h, following the injection of HyP-1. (e) Time-dependent increase in the PA signal of tumor-bearing and control flanks in (d). Adapted from ref. 132. Copyright© 2017 Springer Nature. (f) Design of the PA/NIR-FL dual-mode probe Rhodol-PA and its response mechanism to hNQO1. Adapted from ref. 134. Copyright© 2019 Royal Society of Chemistry. (g) Schematic illustration for the design and mechanism of P-Dex for uPA imaging. Adapted from ref. 138. Copyright©2020 John Wiley and Sons. (h) Mechanism of self-assembly of near-infrared nanoparticles for PA imaging of ALP in the tumor. Adapted from ref. 144. Copyright© 2018 American Chemical Society.

Open Access Article. Published on 24 kovo 2021. Downloaded on 2026-01-19 22:31:07.
This article is licensed under a Creative Commons Attribution-NonCommercial 3.0 Unported Licence.

of the nitroreductase (NTR) will cause many diseases related to hypoxia. Therefore, the detection of NTR activity is very important for the diagnosis and prognosis of hypoxia-related diseases.[130] Unlike the previous utilization of nitroimidazoles as the response part of imaging hypoxia,[131] Chan and colleagues developed a new hypoxia-response sensor containing an *N*-oxide, which could directly generate the corresponding aniline in hypoxia through a one-step two-electron reduction, thereby avoiding interfering signals caused by intermediate products (Fig. 9c).[132] The complex conversion process made it difficult to achieve the imaging of hypoxia on the short-time scale when nitroimidazole was used as the sensing part. Hypoxia probe 1 (HyP-1) synthesized based on this activation mechanism could simultaneously perform PA/ratiometric NIR-FL dual-modal imaging for chronic hypoxia in cancer (Fig. 9d and e) and short-term acute hypoxia. It has great potential to explore the dynamics and spatial complexity of hypoxia ratiometric NIR fluorescent imaging.

Human NAD(P)H: quinone oxidoreductase isozyme 1 (hNQO1) is a member of the NAD(P)H dehydrogenase (quinone) family and encodes a cytoplasmic 2-electron reductase. hNQO1 can transfer NADH (nicotinamide adenine dinucleotide) or NADPH (nicotinamide adenine dinucleotide phosphate) electrons to quinones and then undergo double electron redox reaction to form lower toxic hydroquinones, thus avoiding cell damage.[133] Therefore, it plays an important role in detoxification and metabolism. Recently, Jiang *et al.* designed a new NIR rhodol derivative dye, Rhodol-NIR, by conjugating the core rhodol structure with 4-hydroxybenzaldehyde *via* classic Knoevenagel reaction.[134] It had a large extinction coefficient, low quantum yield, and structural switch from a ring-open form to a closed spirolactone upon esterification. Subsequently, the Rhodol-PA probe was synthesized by cloaking the hydroxyl group by linking the dye to a trimethyl locked quinone propionic acid moiety (Q3) (Fig. 9f). Rhodol-PA was NIR-FL/PA off due to its closed spironolactone structure. Under the action of hNQO1, the probe was de-esterified and its NIR-FL/PA signal recovery was accompanied by the opening of the spiro ring. Rhodol-PA probe allowed high-contrast NIR-FL/PA dual-modal imaging of overexpressed hNQO1 in cancer cells and living tumors.

The urokinase-type plasminogen activator (uPA) may play a very important role in the infiltration and metastasis of malignant tumors.[135] uPA can bind to uPA receptors on the surface of cancer cells and continuously activate plasmin locally to cause the dissolution of the basement membrane and promote the occurrence of metastasis. uPA is overexpressed in invasive breast cancer; thus, it can be used as a biomarker for the detection of invasive breast cancer.[136,137] Pu's group reported a renal-clearable polymeric probe P-Dex, which could detect overexpressed uPA in invasive breast cancer with high specificity and sensitivity by activating NIR-FL/PA dual-mode imaging and then perform effective renal clearance to minimize the potential toxicity.[138] The probe consisted of four components: (1) a renal-clearable promoter, dextran backbone; (2) a signaling moiety, NIR hemicyanine dye (CyN3OH); (3) a self-immolative linker, *p*-aminobenzyl alcohol; (4) a peptide substrate recognized and cleaved by uPA, carbobenzyloxy-Gly-Gly-Arg-OH (Fig. 9g). Initially, the "–OH" of the hemicyanine dye in the P-Dex probe was in the "caged" state, with limited intramolecular charge transfer, which showed no fluorescence and photoacoustic. Under uPA activation, the amide bond of the probe was cleaved and the peptide substrate was cleaved, and then the *p*-aminobenzyl alcohol underwent self-combustion so that the fluorescence and photoacoustic signals of the CyN3OH dye were released to achieve the specific imaging of uPA. Therefore, the polymer molecule was expected to be used for the early detection of invasive breast cancer and the identification of invasive and non-invasive breast cancer so as to implement the corresponding treatment and prognosis according to the malignant degree of the tumor.

As a commonly used biomarker, alkaline phosphatase (ALP) can dephosphorylate the corresponding substrate by hydrolyzing the phosphate monoesters to generate free hydroxyl and phosphate ions. ALP is widely distributed in human organs, most of which are located in the bones and liver, and a small part is located in the kidneys and intestines.[139,140] In addition, the membrane structure of some cancer cells also shows ALP overexpression, such as HepG2, HeLa, Saos-2, and MESSA/Dx5.[141,142] Therefore, some probes used for tumor imaging sometimes contain a hydrolysis site of ALP. When the probe is dephosphorylated to turn on the imaging signal or self-assembly accompanied by a decrease in water solubility, the probe will have an enhanced signal-to-noise ratio and tumor accumulation time based on the enhanced permeability and retention (EPR) effect.[143] Based on this principle, Liang *et. al* developed an ALP-triggered near-infrared photoacoustic probe IR775-Phe-Phe-Tyr(H_2PO_3)-OH (1P).[140] The probe consisted of the NIR dye IR775 for PA imaging and the Phe-Phe-Tyr(H_2PO_3)-OH motif for ALP-triggered self-assembly. The probe could be dephosphorylated under the catalysis of ALP to form IR775-Phe-Tyr-OH and to obtain enhanced hydrophobicity, resulting in self-assembly to generate the nanoparticles (denoted as 1-NPs) (Fig. 9h). 1-NPs with quenched fluorescence signal and enhanced PA signal had been successfully applied for the PA imaging of ALP activity *in vitro* and tumors. Similarly, Lin *et. al* designed and synthesized the first ALP-activated NIR-FL/PA dual-modal probe LET-3, which contained a near-infrared hemicyanide dye (LET-CyOH) and an ALP response site (phosphate).[144] The phosphate moiety could be specifically cleaved by ALP, which led to the enhancement of the electron-donating ability of the oxygen atoms in the molecule and the significant recovery of the FL and PA signals of the LET-CyOH dyes. The probe combined high sensitivity of FL imaging with deep tissue penetration and high spatial resolution of PA imaging. The detection of ALP enzymes *in vitro* showed 23 times FL enhancement at 730 nm and 27 times PA enhancement at 710 nm. Moreover, based on the good biocompatibility of LET-3, it had successfully achieved high sensitivity and selective real-time monitoring of ALP levels in live tumor-bearing mice.

4. Discussion and conclusion

In this review, we surveyed several typical "Always on" and activatable photoacoustic probes based on small-molecule

 © 2021 The Author(s). Published by the Royal Society of Chemistry

Open Access Article. Published on 24 kovo 2021. Downloaded on 2026-01-19 22:31:07.
This article is licensed under a Creative Commons Attribution-NonCommercial 3.0 Unported Licence.

organic dyes in the application in the biomedical field. We also detailed the application of single-function and multifunction photoacoustic probes in PAI and multimodal imaging-guided therapy, as well as the application of activatable photoacoustic probes for the detection of pathological biomarkers, and physiological indexes. Therefore, in view of the advantages of PAI technology and small-molecule contrast agent, PAI based on small-molecule dyes has great potential for development.

Although PAI technology has made great progress in the biomedical field, it also has many deficiencies. For example, a small molecule photoacoustic contrast agent exhibits poor optical and chemical stability. Moreover, the existing small-molecule dyes have a relatively short absorption wavelength (<1000 nm) and the imaging quality is difficult to further improve. Considering the above-mentioned issues, we look forward to the future development of dyes photoacoustic imaging based on small-molecule organic dye.

5. Perspective

1. Several types of conventional photoacoustic probes are prone to photobleaching under long-term laser irradiation, such as cyanine dyes. Therefore, the development of photoacoustic probes with good light stability is important to improve the accuracy of disease diagnosis.

2. Photoacoustic probes based on small-molecule dyes have received widespread attention due to their fast metabolism *in vivo*. However, almost no small molecule dye can be used in the second near-infrared window (NIR-II, 1000–1700 nm) photoacoustic imaging so far. Therefore, the development of small molecule dyes with absorption wavelength above 1000 nm and high molar extinction coefficient is of great significance to further improve the imaging depth and resolution.

3. Improving the active targeting cap ability of photoacoustic probes in lesion location is another question. Most of the existing photoacoustic probes have poor targeting, which lead to false positive signals and reduce the accuracy of disease diagnosis. Hence, it is necessary to enhance the targeting ability of photoacoustic probes.

Conflicts of interest

There are no conflicts to declare.

Acknowledgements

This work was supported by National Natural Science Foundation of China (22022404, 22074050, 21708012, 81600459, 51402099) Wuhan scientific and technological projects (2019020701011441). NSF of Hubei Province (2017CFB151). Finally, thanks to the Research Fund Program of Guangdong Key Laboratory of Radioactive and Rare Resource Utilization (2018B030322009); supported by the Open fund by Jiangsu Key Laboratory of Atmospheric Environment Monitoring and Pollution Control (KHK1909); supported by the State Key Laboratory of Fine Chemicals, Dalian University of Technology (KF 1907).

Notes and references

1 Y. Jin and X. Gao, *Nat. Nanotechnol.*, 2009, **4**, 571–576.
2 M. Rudin and R. Weissleder, *Nat. Rev. Drug Discovery*, 2003, **2**, 123–131.
3 J. Li, Y. Liu, Y. Xu, L. Li, Y. Sun and W. Huang, *Corrd. Chem. Rev.*, 2020, **415**, 213318.
4 M. Won, M. Li, H. S. Kim, P. Liu, S. Koo, S. Son, J. H. Seo and J. S. Kim, *Coord. Chem. Rev.*, 2021, **426**, 213608.
5 J. T. Hou, W. X. Ren, K. Li, J. Seo, A. Shama, X. Q. Yu and J. S. Kim, *Chem. Soc. Rev.*, 2017, **53**, 2076–2090.
6 Q. Miao, C. Xie, X. Zhen, Y. Lyu, H. Duan, X. Liu, J. Jokerst and K. Pu, *Nat. Biotechnol.*, 2017, **35**, 1102–1110.
7 L. Wu, Y. Ishigaki, Y. Hu, K. Sugimoto, W. Zeng, T. Harimoto, Y. Sun, J. He, T. Suzuki, X. Jiang, H. Chen and D. Ye, *Nat. Commun.*, 2020, **11**, 446.
8 L. Nie and X. Chen, *Chem. Sov. Rev.*, 2014, **43**, 7132–7170.
9 H. Zhou, H. Yang, L. Tang, Y. Wang, Y. Li, N. Liu, X. Zeng, Y. Yan, J. Wu, S. Chen, L. Xiao, Y. Yu, Z. Deng, H. Deng, X. Hong and Y. Xiao, *J. Mater. Chem. C*, 2019, **7**, 9448–9454.
10 D. Soliman, G. J. Tserevelakis, M. Omar and V. Ntziachristos, *Sci. Rep.*, 2015, **5**, 12902.
11 L. Tu, Y. Xu, Q. Ouyang, X. Li and Y. Sun, *Chin. Chem. Lett.*, 2019, **30**, 1731–1737.
12 Y. Sun, F. Ding, Z. Zhou, C. Li, M. Pu, Y. Xu, Y. Zhan, X. Lu, H. Li, G. Yang, Y. Sun and P. J. Stang, *Proc. Natl. Acad. Sci. U. S. A.*, 2019, **116**, 1968–1973.
13 G. Hong, A. L. Antaris and H. Dai, *Nat. Biomed. Eng.*, 2017, **1**, 0010.
14 Z. Lei and F. Zhang, *Angew. Chem., Int. Ed.*, 2020, DOI: 10.1002/anie.202007040.
15 P. K. Upputuri and M. Pramanik, *J. Biomed. Opt.*, 2019, **24**, 040901.
16 L. Wang and J. Yao, *Nat. Methods*, 2016, **13**, 627–638.
17 J. Huang and K. Pu, *Angew. Chem., Int. Ed.*, 2020, **59**, 11717–11731.
18 S. Manohar and D. Razansky, *Adv. Opt. Photonics*, 2016, **8**, 586–617.
19 R. Wang, H. Yang, C. Liu, M. Qiu, X. Ma, Z. Mao, Y. Sun and Z. Liu, *Chin. Chem. Lett.*, 2021, **32**, 168–178.
20 H. Chen and G. Diebold, *Science*, 1995, **270**, 963–966.
21 R. E. Borg and J. Rochford, *Photochem. Photobiol.*, 2018, **94**, 1175–1209.
22 Y. Liu, L. Teng, H. Liu, C. Xu, H. Guo, L. Yuan, X. Zhang and W. Tan, *Sci. China: Chem.*, 2019, **62**, 1275–1285.
23 V. Ntziachristos, *Nat. Methods*, 2010, **7**, 603–614.
24 B. Redding, M. A. Choma and H. Cao, *Nat. Photonics*, 2012, **6**, 355–359.
25 I. Steinberg, D. M. Huland, O. Vermesh, H. E. Frostig, W. S. Tummers and S. S. Gambhir, *Photoacoustics*, 2019, **14**, 77–98.
26 Q. Li, S. Li, S. He, W. Chen, P. Cheng, Y. Zhang, Q. Miao and K. Pu, *Angew. Chem., Int. Ed.*, 2020, **132**, 7084–7089.

Open Access Article. Published on 24 kovo 2021. Downloaded on 2026-01-19 22:31:07.
This article is licensed under a Creative Commons Attribution-NonCommercial 3.0 Unported Licence.

27 J. Zhang, X. Zhen, J. Zeng and K. Pu, *Anal. Chem.*, 2018, **90**, 9301–9307.
28 Y. Sun, F. Ding, Z. Chen, R. Zhang, C. Li, Y. Xu, Y. Zhang, R. Ni, X. Li, G. Yang, Y. Sun and P. J. Stang, *Proc. Natl. Acad. Sci. U. S. A.*, 2019, **116**, 16729–16735.
29 R. Zhang, Y. Xu, Y. Zhang, H. S. Kim, A. Sharma, J. Gao, G. Yang, J. S. Kim and Y. Sun, *Chem. Sci.*, 2019, **10**, 8348–8353.
30 R. Zhang, Z. Wang, L. Xu, Y. Xu, Y. Lin, Y. Zhang, Y. Sun and G. Yang, *Anal. Chem.*, 2019, **91**, 12476–12483.
31 A. Yaroslavsky, P. Schulze, I. Yaroslavsky, R. Schober, F. Ulrich and H. Schwarzmaier, *Phys. Med. Biol.*, 2002, **47**, 2059–2073.
32 C. Wu, R. Zhang, W. Du, L. Cheng and G. Liang, *Nano Lett.*, 2018, **18**, 7749–7754.
33 A. Ron, X. L. Deán-Ben, J. Reber, V. Ntziachristos and D. C. Razansky, *Mol. Imaging Biol.*, 2019, **21**, 620–625.
34 J. Huang and K. Pu, *Angew. Chem., Int. Ed.*, 2020, **132**, 11813–11827.
35 Y. Sun, H. Shi, X. Cheng, L. Wu, Y. Wang, Z. Zhou, J. He, H. Chen and D. Ye, *CCS Chem.*, 2020, **2**, 1336–1349.
36 Y. Jiang and K. Pu, *Adv. Biosyst.*, 2018, **2**, 1700262.
37 Kenry, Y. Duan and B. Liu, *Adv. Mater.*, 2018, **30**, 1802394.
38 B. Ding, Y. Xiao, H. Zhou, X. Zhang, C. Qu, F. Xu, Z. Deng, Z. Cheng and X. Hong, *J. Med. Chem.*, 2019, **62**, 2049–2059.
39 Q. Fu, R. Zhu, J. Song, H. Yang and X. Chen, *Adv. Mater.*, 2019, **31**, 1805875.
40 Y. Li, Z. Cai, S. Liu, H. Zhang, S. Wang, J. W. Y. Lam, R. T. K. Kwok, J. Qian and B. Tang, *Nat. Commun.*, 2020, **11**, 1255.
41 X. Li, X. Gao, W. Shi and H. Ma, *Chem. Rev.*, 2014, **114**, 590–659.
42 J. Li, Y. Zhang, P. Wang, L. Yu, J. An, G. Deng, Y. Sun and J. S. Kim, *Coord. Chem. Rev.*, 2021, **427**, 213559.
43 J. Yang and X. Hong, *Sci. China: Chem.*, 2019, **62**, 7–8.
44 B. Li, M. Zhao and F. Zhang, *ACS Mater. Lett.*, 2020, **2**, 905–917.
45 C. J. Reinhardt and J. Chan, *Biochemistry*, 2018, **57**, 194–199.
46 H. Cheng, Y. Li, B. Tang and J. Yoon, *Chem. Soc. Rev.*, 2020, **49**, 21–31.
47 C. Kim, K. Song, F. Gao and L. Wang, *Radiology*, 2010, **255**, 442–450.
48 K. Sano, M. Ohashi, K. Kanazaki, A. Makino, N. Ding, J. Deguchi, Y. Kanada, M. Ono and H. Saji, *Bioconjugate Chem.*, 2017, **28**, 1024–1030.
49 M. Capozza, F. Blasi, G. Valbusa, P. Oliva, C. Cabella, F. Buonsanti, A. Cordaro, L. Pizzuto, A. Maiocchi and L. Poggi, *Photoacoustics*, 2018, **11**, 36–45.
50 S. Wang, G. Yu, Y. Ma, Z. Yang, Y. Liu, J. Wang and X. Chen, *ACS Appl. Mater. Interfaces*, 2019, **11**, 1917–1923.
51 X. Li, Y. Tang, J. Li, X. Hu, C. Yin, Z. Yang, Q. Wang, Z. Wu, X. Lu, W. Hang and Q. Fan, *Chem. Commun.*, 2019, **55**, 5934–5937.
52 F. An, Z. Deng, J. Ye, J. Zhang, Y. Yang, C. Li, C. Heng and X. Zhang, *ACS Appl. Mater. Interfaces*, 2014, **6**, 17985–17992.
53 J. M. Merkes, T. Lammers, R. Kancherla, M. Rueping and S. Banala, *Adv. Opt. Mater.*, 2020, **8**, 1902115.
54 P. Xiang, Y. Shen, J. Shen, Z. Feng, M. Sun, Q. Zhang, S. Li, D. Li, G. Zhang, Z. Wu, Y. Tian, Z. Zhang and X. Tian, *Inorg. Chem. Front.*, 2020, **7**, 2753–2758.
55 M. Frenette, M. Hatamimoslehabadi, S. Bellinger-Buckley, S. Laoui, J. La, S. Bag, S. Mallidi, T. Hasan, B. Bouma, C. Yelleswarapu and J. Rochford, *J. Am. Chem. Soc.*, 2014, **136**, 15853–15856.
56 S. Bellinger, M. Hatamimoslehabadi, S. Bag, F. Mathila, J. La, M. Frenette, S. Laoui, D. J. Szalda, C. Yelleswarapu and J. Rochford, *Chem. – Eur. J.*, 2018, **24**, 906–917.
57 Y. Zhou, D. Wang, Y. Zhang, U. Chitgupi, J. Geng, Y. Wang, Y. Zhang, T. R. Cook, J. Xia and J. F. Lovell, *Theranostics*, 2016, **6**, 688–697.
58 H. Liu, X. Wang, Y. Huang, H. Li, C. Peng, H. Yang, J. Li, H. Hong, Z. Lei, X. Zhang and Z. Li, *ACS Appl. Mater. Interfaces*, 2019, **11**, 30511–30517.
59 K. Shimomura, H. Kai, Y. Nakamura, Y. Hong, S. Mori, K. Miki, K. Ohe, Y. Notsuka, Y. Yamaoka, M. Ishida, D. Kim and H. Furuta, *J. Am. Chem. Soc.*, 2020, **142**, 4429–4437.
60 B. Park, K. M. Lee, S. Park, M. Yun and C. Kim, *Theranostics*, 2020, **10**, 2509–2521.
61 C. Ou, Y. Zhang, W. Ge, L. Zhong, Y. Huang, W. Si, W. Wang, Y. Zhao and X. Dong, *Chem. Commun.*, 2020, **56**, 6281–6284.
62 C. Kim, K. H. Song, F. Gao and L. V. Wang, *Radiology*, 2010, **255**, 442–450.
63 C. Yin, X. Zhen, H. Zhao, Y. Tang, Y. Ji, Y. Lyu, Q. Fan, W. Huang and K. Pu, *ACS Appl. Mater. Interfaces*, 2017, **9**, 12332–12339.
64 K. Cheng, H. Chen, C. H. Jenkins, G. Zhang, W. Zhao, Z. Zhang, F. Han, J. Fung, M. Yang, Y. Jiang, L. Xing and Z. Cheng, *ACS Nano*, 2017, **11**, 12276–12291.
65 M. H. Lee, A. Sharma, M. J. Chang, J. Lee, S. Son, J. L. Sessler, C. Kang and J. S. Kim, *Chem. Soc. Rev.*, 2018, **47**, 28–52.
66 X. Xue, A. Lindstrom and Y. Li, *Bioconjugate Chem.*, 2019, **30**, 1585–1603.
67 H. Huang, W. Song, J. Rieffel and J. F. Lovell, *Front. Phys.*, 2015, **3**, 23.
68 U. Chitgupi and J. F. Lovell, *Biomed. Eng. Lett.*, 2018, **8**, 215–221.
69 V. Gujrati, A. Mishra and V. Ntziachristos, *Chem. Commun.*, 2017, **53**, 4653–4672.
70 Y. Zhang, M. Jeon, L. J. Rich, H. Hong, J. Geng, Y. Zhang, S. Shi, T. E. Barnhart, P. Alexandridis, J. D. Huizinga, M. Seshadri, W. Cai, C. Kim and J. F. Lovell, *Nat. Nanotechnol.*, 2014, **9**, 631–638.
71 N. Beziere and V. Ntziachristos, *J. Nucl. Med.*, 2014, **56**, 323–328.
72 J. F. Lovell, C. S. Jin, E. Huynh, H. Jin, C. Kim, J. L. Rubinstein, W. C. W. Chan, W. Cao, L. V. Wang and G. Zheng, *Nat. Mater.*, 2011, **10**, 324–332.
73 X. Zheng, L. Wang, S. Liu, W. Zhang, F. Liu and Z. Xie, *Adv. Funct. Mater.*, 2018, **28**, 1706507.

 © 2021 The Author(s). Published by the Royal Society of Chemistry

Open Access Article. Published on 24 kovo 2021. Downloaded on 2026-01-19 22:31:07.
This article is licensed under a Creative Commons Attribution-NonCommercial 3.0 Unported Licence.

74 X. Wang, X. Wang, S. Jin, N. Muhammad and Z. Guo, *Chem. Rev.*, 2019, **119**, 1138–1192.
75 J. Xia, C. Kim and J. F. Lovell, *Curr. Drug Targets*, 2015, **16**, 571–581.
76 Q. Wang, B. Xia, J. Z. Xu, X. R. Niu, J. Cai, Q. M. Shen, W. J. Wang, W. Huang and Q. Fan, *Mater. Chem. Front.*, 2019, **3**, 650–655.
77 C. Szabo, H. Ischiropoulos and R. Radi, *Nat. Rev. Drug Discovery*, 2007, **6**, 662–680.
78 Y. Lv, D. Cheng, D. Su, M. Chen, B. Yin, L. Yuan and X. Zhang, *Chem. Sci.*, 2018, **9**, 7606–7613.
79 D. E. Clapham, *Cell*, 2007, **131**, 1047–1058.
80 F. P. Guengerich, *J. Biol. Chem.*, 2009, **284**, 709.
81 R. Yan and D. Ye, *Sci. Bull.*, 2016, **61**, 1672–1679.
82 Z. Luo, L. Feng, R. An, G. Duan, R. Yan, H. Shi, J. He, Z. Zhou, C. Ji, H. Chen and D. Ye, *Chem. – Eur. J.*, 2017, **23**, 14778–14785.
83 X. Zhang and W. Le, *Exp. Neurol.*, 2010, **223**, 299–303.
84 Y. Xu, Y. Zhang, J. Li, J. An, C. Li, S. Bai, A. Sharma, G. Deng, J. S. Kim and Y. Sun, *Biomaterials*, 2020, **259**, 120315.
85 B. A. Webb, M. Chimenti, M. P. Jacobson and D. L. Barber, *Nat. Rev. Cancer*, 2011, **11**, 671–677.
86 A. Fernández and M. Vendrell, *Chem. Soc. Rev.*, 2016, **45**, 1182–1196.
87 Y. Lyu and K. Pu, *Adv. Sci.*, 2017, **4**, 1600481.
88 Q. Miao and K. Pu, *Adv. Mater.*, 2018, **30**, 1801778.
89 L. Teng, G. Song, Y. Liu, X. Han, Z. Li, Y. Wang, S. Huan, X. Zhang and W. Tan, *J. Am. Chem. Soc.*, 2019, **141**, 13572–13581.
90 X. Cheng, R. Sun, L. Yin, Z. Chai, H. Shi and M. Gao, *Adv. Mater.*, 2017, **29**, 1604894.
91 M. H. Lee, A. Sharma, M. J. Chang, J. Lee, S. Son, J. L. Sessler, C. Kang and J. S. Kim, *Chem. Soc. Rev.*, 2018, **47**, 28–52.
92 C. J. Reinhardt and J. Chan, *Biochemistry*, 2018, **57**, 194–199.
93 Q. Ouyang, L. Tu, Y. Zhang, H. Chen, Y. Fan, Y. Tu, Y. Li and Y. Sun, *Anal. Chem.*, 2020, **92**, 14947–14952.
94 B. D'Autréaux and M. Toledano, *Nat. Rev. Mol. Cell Biol.*, 2007, **8**, 813–824.
95 I. Fridovich, *J. Biol. Chem.*, 1997, **272**, 18515–18517.
96 J. M. Merkes, M. Rueping, F. Kiessling and S. Banala, *ACS Sens.*, 2019, **4**, 2001–2008.
97 Y. Zhang and J. F. Lovell, *Theranostics*, 2012, **2**, 905–915.
98 D. Cheng, Y. Pan, L. Wang, Z. Zeng, L. Yuan, X. Zhang and Y. Chang, *J. Am. Chem. Soc.*, 2017, **139**, 285–292.
99 R. Radi, *J. Biol. Chem.*, 2013, **288**, 26464–26472.
100 C. S. Cobbs, T. R. Whisenhunt, D. R. Wesemann, L. E. Harkins, E. G. Van Meir and M. Samanta, *Cancer Res.*, 2003, **63**, 8670–8673.
101 J. Zhang, X. Zhen, J. Zeng and K. Pu, *Anal. Chem.*, 2018, **90**, 9301–9307.
102 X. Zhang, H. Liu, H. Zhang, X. Lou, L. Teng, J. Yuan, L. Yuan and W. Tan, *Chem. Commun.*, 2020, **56**, 8103–8106.
103 R. A. Hunter, W. L. Storm, P. N. Coneski and M. H. Schoenfisch, *Anal. Chem.*, 2013, **85**, 1957–1963.
104 E. Huynh, B. Y. C. Leung, B. L. Helfield, M. Shakiba, J. A. Gandier, C. S. Jin, E. R. Master, B. C. Wilson, D. E. Goertz and G. Zheng, *Nat. Nanotech.*, 2015, **10**, 325–332.
105 S. Wang, Z. Li, Y. Liu, G. Feng, J. Zheng, Z. Yuan and X. Zhang, *Sens. Actuators, B*, 2018, **267**, 403–411.
106 E. K. Patterson, D. D. Fraser, A. Capretta, R. F. Potter and G. Cepinskas, *Free Radical Biol. Med.*, 2014, **70**, 167–173.
107 H. Xiao, K. Xin, H. Dou, G. Yin, Y. Quan and R. Wang, *Chem. Commun.*, 2015, **51**, 1442–1445.
108 Y. Yue, C. Yin, F. Huo, J. Chao and Y. Zhang, *Sens. Actuators, B*, 2014, **202**, 551–556.
109 Z. Wu, X. Wu, Z. Li, Y. Yang, J. Han and S. Han, *Bioorg. Med. Chem. Lett.*, 2013, **23**, 4354–4357.
110 T. Ikeno, K. Hanaoka, S. Iwaki, T. Myochin, Y. Murayama, H. Ohde, T. Komatsu, T. Ueno, T. Nagano and Y. Urano, *Anal. Chem.*, 2019, **91**, 9086–9092.
111 G. I. Giles, K. M. Tasker and C. Jacob, *Free Radical Biol. Med.*, 2001, **31**, 1279–1283.
112 L. Yuan, W. Lin, K. Zheng, L. He and W. Huang, *Chem. Soc. Rev.*, 2013, **42**, 622–661.
113 L. Wu, Y. Sun, K. Sugimoto, Z. Luo, Y. Ishigaki, K. Pu, T. Suzuki, H. Chen and D. Ye, *J. Am. Chem. Soc.*, 2018, **140**, 16340–16352.
114 V. Lin, W. Chem, M. Xiao and C. Chang, *Chem. Soc. Rev.*, 2015, **44**, 4596–4618.
115 K. Kondo, S. Bhushan, A. L. King, S. D. Prabhu, T. Hamid, S. Koenig, T. Murohara, B. L. Predmore, G. Gojon Sr, G. Gojon Jr, R. Wang, N. Karusula, C. K. Nicholson, J. W. Calvert and D. J. Lefer, *Circulation*, 2013, **127**, 1116–1127.
116 B. D. Paul, J. I. Sbodio, R. Xu, M. S. Vandiver, J. Y. Cha, A. M. Snowman and S. H. Snyder, *Nature*, 2014, **509**, 96–100.
117 B. Shi, X. Gu, Q. Fei and C. Zhao, *Chem. Sci.*, 2017, **8**, 2150–2155.
118 G. Yin, T. Niu, T. Yu, Y. Gan, X. Sun, P. Yin, H. Chen, Y. Zhang, H. Li and S. Yao, *Angew. Chem., Int. Ed.*, 2019, **58**, 4557–4561.
119 J. B. Schulz, J. Lindenau, J. Seyfried and J. Dichgans, *Eur. J. Biochem.*, 2000, **267**, 4904–4911.
120 W. Gao, X. Li, Z. Liu, W. Fu, Y. Sun, W. Cao, L. Tang and B. Tang, *Anal. Chem.*, 2019, **91**, 1150–1156.
121 K. G. Reddie and K. S. Carroll, *Curr. Opin. Chem. Biol.*, 2008, **12**, 746–754.
122 G. Yin, T. Niu, Y. Gan, T. Yu, P. Yin, H. Chen, Y. Zhang, H. Li and S. Yao, *Angew. Chem., Int. Ed.*, 2018, **57**, 4991–4994.
123 B. D. Paul, J. I. Sbodio and S. H. Snyder, *Trends Pharmacol. Sci.*, 2018, **39**, 513–524.
124 H. Wang, Y. Zhang, Y. Yang, Z. He, C. Wu, W. Zhang, W. Zhang, J. Liu, P. Li and B. Tang, *Chem. Commun.*, 2019, **55**, 9685–9688.
125 P. Zhang, X. Nie, M. Gao, F. Zeng, A. Qin, S. Wu and B. Tang, *Mater. Chem. Front.*, 2017, **1**, 838–845.
126 Z. Luo, R. An and D. Ye, *ChemBioChem*, 2019, **20**, 474–487.

Open Access Article. Published on 24 kovo 2021. Downloaded on 2026-01-19 22:31:07.
This article is licensed under a Creative Commons Attribution-NonCommercial 3.0 Unported Licence.

127 S. Shalini, L. Dorstyn, S. Dawar and S. Kumar, *Cell Death Differ.*, 2014, **22**, 526–539.
128 P. Ray, A. De, M. Patel and S. S. Gambhir, *Clin. Cancer Res.*, 2008, **14**, 5801–5809.
129 Y. Wang, X. M. Hu, J. Weng, J. Li, Q. Fan, Y. Zhang and D. Ye, *Angew. Chem., Int. Ed.*, 2019, **131**, 4940–4944.
130 G. L. Semenza, *Annu. Rev. Pathol.*, 2014, **9**, 47–71.
131 K. A. Krohn, J. M. Link and R. P. Mason, *J. Nucl. Med.*, 2008, **49**, 129S–148S.
132 H. J. Knox, J. Hedhli, T. W. Kim, K. Khalili, L. W. Dobrucki and J. Chan, *Nat. Commun.*, 2017, **8**, 1794.
133 N. Kwon, M. K. Cho, S. J. Park, D. Kim, S. J. Nam, L. Cui, H. M. Kim and J. Yoon, *Chem. Commun.*, 2017, **53**, 525–528.
134 F. Liu, X. Shi, X. Liu, F. Wang, H. B. Yi and J. H. Jiang, *Chem. Sci.*, 2019, **10**, 9257–9264.
135 Y. Xu, M. Tian, H. Zhang, Y. Xiao, X. Hong and Y. Sun, *Chin. Chem. Lett.*, 2018, **29**, 1093–1097.
136 S. Huang, P. K. Upputuri, H. Liu, M. Pramanik and M. Wang, *J. Mater. Chem. B*, 2016, **4**, 1696–1703.
137 J. L. Fisher, P. S. Mackie, M. L. Howard, H. Zhou and P. F. Choong, *Clin. Cancer Res.*, 2001, **7**, 1654–1660.
138 Q. Li, S. Li, S. He, W. Chen, P. Cheng, Y. Zhang, Q. Miao and K. Pu, *Angew. Chem., Int. Ed.*, 2020, **59**, 7018–7023.
139 F. Sacco, L. Perfetto, L. Castagnoli and G. Cesareni, *FEBS Lett.*, 2012, **586**, 2732–2739.
140 C. Wu, R. Zhang, W. Du, L. Cheng and G. Liang, *Nano Lett.*, 2018, **18**, 7749–7754.
141 W. Tang, Z. Zhao, Y. Chong, C. Wu, Q. Liu, J. Yang, R. Zhou, Z. Lian and G. Liang, *ACS Nano*, 2018, **12**, 9966–9973.
142 J. Stebbing, L. C. Lit, H. Zhang, R. S. Darrington, O. Melaiu, B. Rudraraju and G. Giamas, *Oncogene*, 2014, **33**, 939–953.
143 Z. Feng, H. Wang, X. Chen and B. Xu, *J. Am. Chem. Soc.*, 2017, **139**, 15377–15384.
144 X. Gao, G. Ma, C. Jiang, L. Zeng, S. Jiang, P. Huang and J. Lin, *Anal. Chem.*, 2019, **91**, 7112–7117.

 © 2021 The Author(s). Published by the Royal Society of Chemistry